

Revisiting Rolling Shutter Bundle Adjustment: Toward Accurate and Fast Solution

Bangyan Liao[†], Delin Qu[†], Yifei Xue, Huiqing Zhang, and Yizhen Lao^{*}

Abstract—We propose a robust and fast bundle adjustment solution that estimates the 6-DoF pose of the camera and the geometry of the environment based on measurements from a rolling shutter (RS) camera. This tackles the challenges in the existing works, namely relying on additional sensors, high frame rate video as input, restrictive assumptions on camera motion, readout direction, and poor efficiency. To this end, we first investigate the influence of normalization to the image point on RSBA performance and show its better approximation in modelling the real 6-DoF camera motion. Then we present a novel analytical model for the visual residual covariance, which can be used to standardize the reprojection error during the optimization, consequently improving the overall accuracy. More importantly, the combination of normalization and covariance standardization weighting in RSBA (*NW-RSBA*) can avoid common planar degeneracy without needing to constrain the filming manner. Besides, we propose an acceleration strategy for *NW-RSBA* based on the sparsity of its Jacobian matrix and Schur complement. The extensive synthetic and real data experiments verify the effectiveness and efficiency of the proposed solution over the state-of-the-art works. We also demonstrate the proposed method can be easily implemented and plug-in famous GSfM and GSSLAM systems as completed RSSfM and RSSLAM solutions.

Index Terms—Bundle adjustment, Rolling Shutter, Distortion correction

1 INTRODUCTION

BUNDLE adjustment (BA) is the problem of simultaneously refining the camera's relative motion and the observed points in the scene, by minimizing the reprojection errors over images and points [1]. It has made a great success in the past two decades as a vital step for two 3D computer vision applications: structure-from-motion (SfM) and simultaneous localization and mapping (SLAM). Thus, BA has various practical applications in scene modelling [2], 3D mapping [3], augmented reality [4] and robot navigation [5].

CMOS cameras have been widely equipped with rolling shutters (RS) due to their inexpensive cost, low energy consumption, superior resolution, and higher frame rate. However, in comparison with its global shutter (GS) counterpart, RS cameras are exposed in a scanline-by-scanline fashion. Consequently, images captured by moving RS cameras produce image distortions known as the RS effect [6], which can severely defeat vital steps (e.g. absolute [7] and relative [8] pose estimation) in SfM and SLAM, including BA [9], [10], [11], [12], [13]. Hence, handling the RS effect in BA (RSBA) is necessary to achieve more accurate performance.

1.1 Related Work

One of the critical issues in solving RSBA is assuming a model of instantaneous camera motion and optimizing its state vectors together with geometry parameters in the

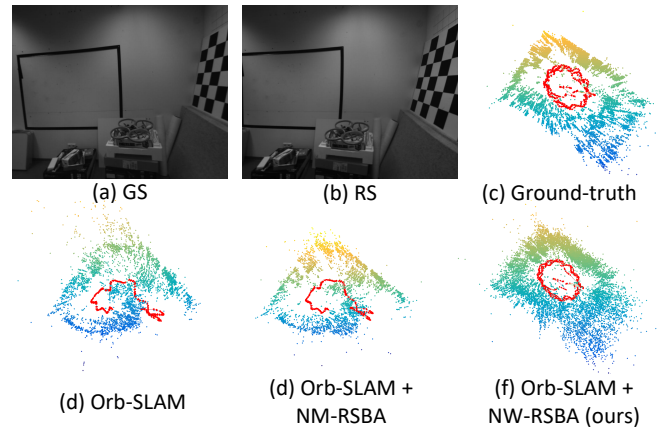


Fig. 1: Images were captured at the same time with fast motion with (a) global shutter and (b) rolling shutter in sequence 10 of the TUM-RSfM dataset [14]. (c) classical Orb-SLAM [15] with GS input. (d) classical Orb-SLAM [15] with RS input. (e) Orb-SLAM augmented with NM-RSBA [11]. (f) Orb-SLAM augmented with proposed NW-RSBA.

framework of BA. The state-of-the-art works for RSBA can be divided into five main classes:

Video-based Methods. Hedborg et al. [16] use an RS video sequence to solve RSSfM and present an RSBA algorithm adapted to smooth motion between consecutive frames assumption in [9]. Similarly, Im et al. [10] propose a small motion interpolation and BA algorithm specifically for narrow-baseline RS image sequences. Zhuang et al. [17] further address this setting by presenting 8pt and 9pt linear solvers, which are developed to recover the relative pose of an RS

• D. Qu, B. Liao, H. Zhang and Y. Lao are with the College of Computer Science and Electronic Engineering, Hunan University, Changsha, China, 410082.

• Y. Xue is with Jiangxi Provincial Natural Resources Cause Development Center, China.

[†] Authors contributed equally

^{*} Corresponding author

E-mail: yizhenlao@hnu.edu.cn

Manuscript received XXXXXX.

camera that undergoes constant velocity and acceleration motion, respectively. Different from the linear interpolation in [9], [10], [17], a spline-based trajectory model to better reformulate the motion between frames is proposed by [18]. Oth et al. [19] present a new method for rolling shutter calibration that only requires a video of a known pattern based on continuous-time estimation.

All the video-based methods rely on the assumption that the high frame rate video provides spatial-temporal consecutive images which can be used to interpolate the pose of each scanline, namely modelling RS projection.

Gyroscope-based Methods. The works of [5], [20] present an SfM solution to mobile phone RS videos by fusion with an inertial measurement unit (IMU). RSSfM in Large-scale scenes has been addressed by [21], [22] with the exploitation of good relative pose prior by using additional sensors such as GPS and IMU. Recently, the work of [23] proposes a spline error weighting scheme for visual-inertial fusion on RS video.

Most gyroscope-based methods rely on the high frame rate video sequence input with precise calibration between IMU and camera. Considering the energy-intensive setup, they remain unsuitable as a solution.

Stereo-based Methods. Ait-Aider et al. [24] firstly studied the calibrated RS stereo system and present a method for object structure and kinematics estimation using iterative optimization. Saurer et al. [25] propose a stereo RSSfM under pure translation instantaneous-motion model.

Matter of fact, stereo-based methods require stereo configuration with precise pre-calibration, which is typically unattainable.

Unordered RSBA. An unordered image set is the standard input for SfM. Albl et al. [11] address the unordered RSSfM problem and point out the typical degeneration configuration of RSSfM. Ito et al. [12] attempt to solve RSSfM by establishing an equivalence with self-calibrated SfM based on the pure rotation instantaneous-motion model and affine camera assumption, while the work of [26] draws the equivalence between RSSfM and non-rigid SfM for general 6-DoF camera motion. A camera-based RSBA (C-RSBA) algorithm has been proposed in Lao [13] in order to avoid the degeneration solution reported in [11].

Direct Methods. Unlike the feature-based BA methods described above, which minimize reprojection errors of keypoints, photometric-based BA methods maximize the photometric consistency among each pair of frames instead (e.g. [27], [28]). To handle the RS effect, the works of [29] and [30] present direct semi-dense and direct sparse SLAM pipelines, respectively.

It is crucial to notice that direct methods heavily rely on the assumption of constant grayscale values among consecutive frames, necessitating photometric calibration in advance [31]. Besides, similar to video-based ones, direct methods also require video sequences as input to hold the constant grayscale assumption.

1.2 Motivations

Although existing works of RSBA have shown promising results, we argue that they generally lead to either highly complex constraints on inputs, time-consuming, or overly restrictive motion models which limit application fields.

More general: 1) Video-based [9], [10], [17], [18] and direct methods [29], [30] that use video sequence as input are often not desirable to be processed frame by frame. This imposes a high acquisition frame rate, resulting in high computational power requirements. 2) Unordered image set is the typical input for classical SfM pipeline (e.g. [3]). 3) Even the BA step in current popular SLAM systems (e.g. [15]) only optimizes keyframes instead of all the consecutive frames, which makes the interpolation scheme presented in video-based and direct methods infeasible. RSBA, on the other hand, which accepts generally unordered image sets as input, is preferable for both RSSfM and RSSLAM.

More effective: 1) Despite the fact that the probability-based weighting algorithm has been verified [15] can successfully improve the BA performance by weighting the error terms. Surprisingly, such a scheme has never been applied to solve the unordered RSBA problem in [11], [12], [13], [26]. 2) Another common case was pointed out by [11] that when the input images are taken with similar readout directions, BA with the RS model fails to recover structure and motion. The proposed solution is simply to avoid the critical configurations by taking images with close to perpendicular readout directions. This solution considerably limits the use in common scenarios. Another noticeable approach to avoid such degeneration solutions is by fusing the information of IMU and video sequence in continuous-time RSBA [18], [23]. Thus, a novel RSBA solution that improves effectiveness and avoids the degeneration solution using exclusively unordered image data with no specific priors (e.g. readout directions) is desirable.

More efficient: GSBA argumentation with the RS motion model has been reported as time-consuming, except the work of [9] investigates using Schur complement to accelerate the video-based RSBA. However, the acceleration of unordered RSBA has never been addressed in the existing works [11], [12], [13], [26]. To bolster the RSSLAM, a more efficient RSBA is in demand.

In summary, an **accurate** and **fast** solution to unordered images RSBA without camera motion assumptions, readout direction, or projection model is still missing. Such a method would be an essential step in the potential widespread deployment of 3D vision with RS imaging systems.

1.3 Contributions

In this paper, we present a novel RSBA solution and tackle the challenges that remained in the previous works, including additional sensors requirement, high frame rate video as input, camera motion assumptions, readout direction constraints, and poor efficiency. To this end, we investigate the influence of normalization to the image point on RSBA performance and show its better approximation in modelling the actual 6-DoF camera motion. Then we present a novel analytical model for the visual residual covariance, which can be used to standardize the reprojection

error during the BA, consequently improving the overall accuracy. More importantly, the combination of normalization and covariance standardization weighting in RSBA can avoid common planar degeneracy without constraining the capture manner. Besides, we propose an acceleration strategy based on sparsity of the Jacobian matrix and Schur complement.

We demonstrate that the proposed method can be easily implemented and plugin GSSfM and GSSLAM systems as completed RSSfM and RSSLAM solutions. The extensive synthetic and real data experiments verify the effectiveness and efficiency of the proposed solution over the state-of-the-art works. The code will be **publicly** available to the community after acceptance.

In summary, the main contributions of this paper are:

- We first thoroughly investigate image point normalization's influence on RSBA and propose a probability-based weighting algorithm in the cost function to improve RSBA performance. We apply these two insights in the proposed RSBA solution named NW-RSBA and present its corresponding acceleration method.
- The proposed RSBA solution NW-RSBA can easily plugin multiple existing GSSfM and GSSLAM solutions to handle the RS effect.
- We verify experimentally that the proposed solution provides more accurate results and $10\times$ speedup over the existing works and avoids degenerate solutions with the usual camera capture manner.

2 FORMULATION OF ROLLING SHUTTER BUNDLE ADJUSTMENT (RSBA)

2.1 RS Projection Model

Direct measurement based RS model: Assuming a 3D point $\mathbf{P}_i = [X_i \ Y_i \ Z_i]^\top$ is observed by a RS camera j represented by measurement \mathbf{m}_i^j in the image domain. The projection model of a 3D point in world frame into image domain in camera frame can be defined as:

$$\begin{bmatrix} \mathbf{m}_i^j & 1 \end{bmatrix}^\top = \begin{bmatrix} u_i^j & v_i^j & 1 \end{bmatrix}^\top = \Pi(\mathbf{K}\mathbf{P}_i^c) \quad (1)$$

$$\mathbf{P}_i^c = [X_i^c \ Y_i^c \ Z_i^c]^\top = \mathbf{R}^j(v_i^j)\mathbf{P}_i + \mathbf{t}^j(v_i^j) \quad (2)$$

where \mathbf{P}_i^c is the 3D point in the camera frame while $\Pi([X \ Y \ Z]^\top) = \frac{1}{Z}[X \ Y]^\top$ is the perspective division. \mathbf{K} is the perspective intrinsic matrix [1]. $\mathbf{R}^j(v_i^j) \in \mathbb{SO}(3)$ and $\mathbf{t}^j(v_i^j) \in \mathbb{R}^3$ define the camera pose when the row index of measurement v_i^j is acquired. Assuming constant camera motion during frame capture, the instantaneous-motion is modelled by:

$$\mathbf{R}^j(v_i^j) = (\mathbf{I} + [\omega^j]_\times v_i^j)\mathbf{R}_0^j \quad \mathbf{t}^j(v_i^j) = \mathbf{t}_0^j + \mathbf{d}^j v_i^j \quad (3)$$

with,

$$\omega^j t_\times = \begin{bmatrix} 0 & -\omega_z^j & \omega_y^j \\ \omega_z^j & 0 & -\omega_x^j \\ -\omega_y^j & \omega_x^j & 0 \end{bmatrix} \quad (4)$$

\mathbf{t}_0^j , \mathbf{R}_0^j is the translation and rotation matrix when the first-row measurement index is observed. While $\mathbf{d}^j =$

$[d_x^j, d_y^j, d_z^j]^\top$ is the linear velocity vector, $\omega^j = [\omega_x^j, \omega_y^j, \omega_z^j]^\top$ is the angular velocity vector. Such linear instantaneous-motion approximation was adopted by [8], [11], [26].

It is important to notice that RS instantaneous-motion is a function of v_i^j , which we named the measurement-based RS model. It has been widely used in existing works [10], [13], [16], [24], [32], [33], [34], [35].

Normalized measurement based RS model: By assuming the pre-calibrated camera, one can transform a image measurement \mathbf{m}_i^j with \mathbf{K} to the normalized measurement coordinate $[\mathbf{q}_i^j \ 1]^\top = \mathbf{K}^{-1}\mathbf{m}_i^j$. Thus, the projection model in Eq. (1) becomes:

$$\begin{bmatrix} \mathbf{q}_i^j & 1 \end{bmatrix}^\top = \begin{bmatrix} c_i^j & r_i^j & 1 \end{bmatrix}^\top = \Pi(\mathbf{R}^j(r_i^j)\mathbf{P}_i + \mathbf{t}^j(r_i^j)) \quad (5)$$

while the camera instantaneous-motion becomes:

$$\mathbf{R}^j(r_i^j) = (\mathbf{I} + [\omega^j]_\times r_i^j)\mathbf{R}_0^j \quad \mathbf{t}^j(r_i^j) = \mathbf{t}_0^j + \mathbf{d}^j r_i^j \quad (6)$$

In contrast to direct-measured based RS model, \mathbf{t}_0^j and \mathbf{R}_0^j is the translation and rotation of the camera optical centre row and ω^j , \mathbf{d}^j are scaled by camera focal length. We name such modelling as normalized measurement RS model, which was used in [9], [11], [12], [17].

2.2 Bundle Adjustment with RS Model

As we argue in section. 1.2 that BA with independent RS models is more general than video-based RSBA. Assuming that cameras index set \mathcal{F} has m cameras, 3D points index set \mathcal{P} owns n points. Non-linear least squares optimizer (e.g. Gauss-Newton) are used to find a solution θ^{j*} of camera poses $\mathbf{R}^{j*}, \mathbf{t}^{j*}$, instantaneous-motion $\omega^{j*}, \mathbf{d}^{j*}$ and 3D points \mathbf{P}_i^* by minimizing the reprojection error \mathbf{e}_i^j over all the visible projections from points to cameras as:

$$\theta^* = \{\mathbf{P}^*, \mathbf{R}^*, \mathbf{t}^*, \omega^*, \mathbf{d}^*\} = \arg \min_{\theta} \sum_{j \in \mathcal{F}} \sum_{i \in \mathcal{P}_j} \|\mathbf{e}_i^j\|^2 \quad (7)$$

where the point set $\mathcal{P}_j \in \mathcal{P}$ is the subset of \mathcal{P} contains all points index observed in camera frame i . There are three categories definitions of \mathbf{e}_i^j used in the previous works:

(1) Direct-Measurement based: Duchamp et al. in [33] use the measurement row index v_i^j of \mathbf{m}_i^j to model the camera pose and compute the reprojection error:

$$\mathbf{e}_i^j = \mathbf{m}_i^j - \Pi(\mathbf{K}(\mathbf{R}^j(v_i^j)\mathbf{P}_i + \mathbf{t}^j(v_i^j))) \quad (8)$$

We name this strategy *DM-RSBA*.

(2) Normalized measurement based: Albl et al. [11] use the normalized measurement row index r_i^j of \mathbf{q}_i^j to model the camera pose and compute the reprojection error:

$$\mathbf{e}_i^j = \mathbf{q}_i^j - \Pi(\mathbf{R}^j(r_i^j)\mathbf{P}_i + \mathbf{t}^j(r_i^j)) \quad (9)$$

We name this strategy *NM-RSBA*.

(3) Camera base: Lao et al. [13] argue both two measurement-based methods in Eq. 8 [33] and Eq. 9 [11] use the row index of image measurement which can not simulate the physical projection process in real world and thus have more possibilities lead to a planar degenerate

Algorithm 1: Normalized Weighted RSBA

Input : Initial rolling shutter camera poses $\{\mathbf{R}^1, \mathbf{t}^1, \omega^1, \mathbf{d}^1\}, \dots, \{\mathbf{R}^j, \mathbf{t}^j, \omega^j, \mathbf{d}^j\}$, points $\mathbf{P}_1, \dots, \mathbf{P}_i$ as θ and point measurement in normalized image coordinate $\mathbf{q}_{1 \dots i}^{1 \dots j}$

Output: Refined parameters θ^*

```

1 while (not reach max iteration) and (not satisfy stopping
  criteria) do
2   for Each camera  $j \in \mathcal{F}$  do
3     for Each point  $i \in \mathcal{P}_j$  do
4       Calculate weighted reprojection error  $\hat{\mathbf{e}}_i^j$ 
        using Alg. 2;
5       Construct Jacobian matrix  $\mathbf{J}_i^j$  using Alg. 3;
6       Parallel connect  $\mathbf{J}_i^j$  to  $\mathbf{J}$  using Eq. (20);
7       Stack  $\hat{\mathbf{e}}_i^j$  into  $\hat{\mathbf{e}}$ ;
8     end
9   end
10  Solve normal equation  $\mathbf{J}^\top \mathbf{J} \delta = -\mathbf{J}^\top \hat{\mathbf{e}}$  using
    Alg. 4;
11  Update camera poses and points parameters  $\theta$ 
    using  $\delta$ ;
12 end

```

solution. In contrast, [13] proposes a camera-based approach that only uses camera pose and instantaneous motion to compute the reprojection error instead of either v_i^j or r_i^j :

$$\mathbf{e}_i^j = \mathbf{m}_i^j - \left[\frac{(\mathbf{K}\mathbf{R}^j)^{(1)}\mathbf{P}_i + \hat{\mathbf{R}}^{j(1)}\mathbf{P}_i v_i^j + (\mathbf{K}\mathbf{t}^j)^{(1)} + (\mathbf{K}\mathbf{d}^j)^{(1)}v_i^j}{(\mathbf{K}\mathbf{R}^j)^{(3)}\mathbf{P}_i + \hat{\mathbf{R}}^{j(3)}\mathbf{P}_i v_i^j + (\mathbf{K}\mathbf{t}^j)^{(3)} + (\mathbf{K}\mathbf{d}^j)^{(3)}v_i^j} \right] \quad (10)$$

with,

$$\begin{aligned} a &= \hat{\mathbf{R}}^{j(3)}\mathbf{P}_i + (\mathbf{K}\mathbf{d}^j)^{(3)} \\ b &= (\mathbf{K}\mathbf{R}^j)^{(3)}\mathbf{P}_i + (\mathbf{K}\mathbf{t}^j)^{(3)} - \hat{\mathbf{R}}^{j(2)}\mathbf{P}_i - (\mathbf{K}\mathbf{d}^j)^{(2)} \\ c &= -(\mathbf{K}\mathbf{R}^j)^{(2)}\mathbf{P}_i - (\mathbf{K}\mathbf{t}^j)^{(2)} \quad \hat{\mathbf{R}}^j = \mathbf{K}[\omega^j]_{\times} \mathbf{R}^j \end{aligned}$$

where $\mathbf{M}^{(r)}$ is the r^{th} row of matrix \mathbf{M} . a , b and c are three auxiliary variables while $\hat{\mathbf{R}}^j$ is an auxiliary matrix. We name this strategy DC-RSBA.

3 METHODOLOGY

To tackle the challenges remained in the existing works, we propose a novel RSBA algorithm called normalized weighted RSBA (*NW-RSBA*). The main idea is to use measurement normalization (section. 3.1) and covariance standardization weighting (section. 3.2) jointly during the optimization. Besides, we provide a two-stage Schur complement strategy to accelerate *NW-RSBA* in section. 3.3. Algorithm. 1 shows the pipeline of *NW-RSBA*.

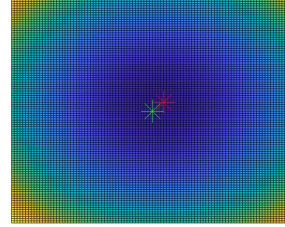
The main differences between *NW-RSBA* and existing methods [11], [13], [33] are summarized in table. 1.

3.1 Measurement Normalization

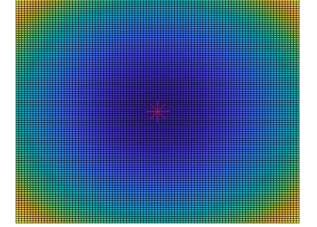
Though both direct measurement (Eq. (8) and (10)) and normalized measurement (Eq. (9)) were used as optimization objective functions in the existing works. But to the best

TABLE 1: Comparison of the proposed *NW-RSBA* and existing general unordered RSBA methods [11], [13], [33]. N: normalized image measurement; D: direct image measurement without normalization; M-based: measurement-based projection model; C-based: camera-based projection model.

	DM RSBA [33]	NM RSBA [11]	DC RSBA [13]	NW RSBA
Normalization	D	N	D	N
Reprojecting computation	M-based	M-based	C-based	M-based
Analytical Jacobian	×	✓	×	✓
BA acceleration	×	×	×	✓



(a) DM-RSBA



(b) NM-RSBA

Fig. 2: Reprojection loss surface of (a) *DM-RSBA* [33] and (b) *NM-RSBA* [11] under the same configuration. The x-axis and y-axis are d_x^j and d_y^j of camera motion respectively. The green stars are the ground truth solutions while the red stars are the minimums in loss surfaces. Notice that *DM-RSBA* has a biased minimum while the minimum of *NW-RSBA* exactly coincides with the ground truth one.

of our knowledge, no work has investigated the influence of normalization on the RSBA performance before. Thus, we conduct a synthetic experiment to evaluate the impact of normalization by comparing the performances of *DM-RSBA* [33], *NM-RSBA* [11]. The results in Fig. 8 show that the normalization significantly improves the RSBA accuracy. We interpret this improvement for two reasons:

- **Better instantaneous-motion approximation:** The instantaneous-motion approximation can be seen as a low-order approximation to the Taylor expansion of real motion. Therefore, the higher-order residual term grows with the increase of the row index. This residual may be non-negligible once the row index is huge and leads to a biased convergence basin. Thus, with the residual quadratic growth, the minimum point in the loss surface may shift over the ground truth to equally distribute the error among all observations. However, with the quadratic growth, the magnitude of the normalized RS model's biggest residual is much smaller than the direct one. A direct proof shown in Fig. 2 verifies our insight that *NM-RSBA* has an unbiased minimum over *DM-RSBA*.
- **Faster convergence:** Note that GS-based pose estimation and triangulation provide the initialization to RSBA. In order to average the errors among images, the initialized pose intends to be closer to the pose of the middle row. Such initialization is thus closer to *NM-*

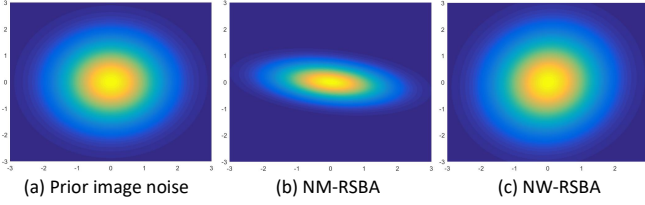


Fig. 3: Monte Carlo simulation to the covariance of (a) prior Gaussian image noise, error term of (b) NM-RSBA [11], and the proposed (c) NW-RSBA. Notice that NW-RSBA re-scales the covariance ellipse back to a unit one.

Algorithm 2: Computation of weighted reprojection error $\hat{\mathbf{e}}_i^j$

Input : Rolling shutter camera poses $\{\mathbf{R}^j, \mathbf{t}^j, \omega^j, \mathbf{d}^j\}$, points \mathbf{P}_i and point measurement in normalized image coordinate \mathbf{q}_i^j

Output: Normalized weighted error $\hat{\mathbf{e}}_i^j$

- 1 Compute weight matrix \mathbf{C}_i^j using Eq. (12a);
 - 2 Compute standard reprojection error \mathbf{e}_i^j using Eq. (9);
 - 3 Return normalized weighted reprojection error $\hat{\mathbf{e}}_i^j$ using Eq. (19);
-

RSBA, which also uses the pose of the middle row as an anchor, while far from DM-RSBA, which uses the pose of the first row instead.

Therefore, we propose to **normalize the measurements** before RSBA.

3.2 Normalized Weighted RSBA

Based on the measurement normalization, we further present a normalized weighted RSBA (NW-RSBA) by modelling image noise covariance.

Weighting the reprojection error: In contrast to existing works [11], [13], [33], we consider the image noise in RSBA by weighting the squared reprojection error $\|\mathbf{e}_i^j\|^2$ with inverse covariance matrix of the error Σ_i^{j-1} . This strategy is also known as standardisation of the error terms, which aims at scaling every term by its inverse covariance matrix and ends up with isotropic covariance [36].

Following section. 2.2, the cost function in Eq. (7) becomes:

$$\theta^* = \arg \min_{\theta} \sum_{j \in \mathcal{F}} \sum_{i \in \mathcal{P}_j} \mathbf{e}_i^j \Sigma_i^{j-1} \mathbf{e}_i^j \quad (11)$$

where $\theta^* = \{\mathbf{P}^*, \mathbf{R}^*, \mathbf{t}^*, \omega^*, \mathbf{d}^*\}$, and \mathbf{e}_i^j is the reprojection error computed by normalized measurement based approach described in Eq. (9). By assuming the image measurement \mathbf{q}_i^j follows a prior statistically independent Gaussian noise: $\mathbf{n}_i^j \sim \mathcal{N}(0, \mathbf{W}\Sigma\mathbf{W}^\top)$. The newly introduced covariance matrix of the error Σ_i^j is defined as

$$\Sigma_i^j = \mathbf{C}_i^j \mathbf{W} \Sigma \mathbf{W}^\top \mathbf{C}_i^{j\top} \quad (12)$$

with,

$$\mathbf{C}_i^j = \begin{bmatrix} 1 & 0 \\ 0 & 1 \end{bmatrix} - \begin{bmatrix} \frac{1}{Z^{c_j^j}} & 0 \\ 0 & \frac{1}{Z^{r_j^j}} \\ \frac{-X^{c_j^j}}{Z^{c_j^j 2}} & \frac{-Y^{r_j^j}}{Z^{r_j^j 2}} \end{bmatrix}^\top ([\omega^j]_\times \mathbf{R}^j \mathbf{P}_i + \mathbf{d}^j) \begin{bmatrix} 0 & 1 \end{bmatrix} \quad (12a)$$

$$\mathbf{W} = \begin{bmatrix} 1/f_x & 0 \\ 0 & 1/f_y \end{bmatrix} \quad (12b)$$

where \mathbf{C}_i^j is an 2×2 auxiliary matrix. \mathbf{W} is also an fixed 2×2 auxiliary matrix defined by the focal lengths f_x and f_y in pre-calibrated \mathbf{K} .

Thus, we can compute the weighted reprojection error following the Alg. 2.

• **Proof. of Eq. (12).** Let normalized measurement \mathbf{q}_i^j be the perfect measurement $\tilde{\mathbf{q}}_i^j$ integrate with normalized image noise $[n_c \ n_r]^\top$.

$$\begin{bmatrix} c & r \end{bmatrix}^\top = [\tilde{c} \ \tilde{r}]^\top + [n_c \ n_r]^\top \quad (13)$$

with, $\begin{bmatrix} n_c & n_r \end{bmatrix}^\top \sim \mathcal{N}(0, \mathbf{W}\Sigma\mathbf{W}^\top)$

then we can model the reprojection error \mathbf{e}_i^j between the perfect projection and reprojection using a normalized measurement based approach in Eq. (9) as:

$$\begin{aligned} \mathbf{e}_i^j &= \begin{bmatrix} c_i^j & r_i^j \end{bmatrix}^\top - \Pi(\mathbf{R}^j(r_i^j)\mathbf{P}_i + \mathbf{t}^j(r_i^j)) \\ &= \begin{bmatrix} c_i^j & r_i^j \end{bmatrix}^\top - \Pi(\mathbf{R}^j(\tilde{r}_i^j + n_r)\mathbf{P}_i + \mathbf{t}^j(\tilde{r}_i^j + n_r)) \end{aligned} \quad (14)$$

where $\Pi(\mathbf{R}^j(\tilde{r}_i^j + n_r)\mathbf{P}_i + \mathbf{t}^j(\tilde{r}_i^j + n_r))$ can be linearized using the Taylor first order approximation:

$$\begin{aligned} &\Pi(\mathbf{R}^j(\tilde{r}_i^j + n_r)\mathbf{P}_i + \mathbf{t}^j(\tilde{r}_i^j + n_r)) \\ &= \begin{bmatrix} \tilde{c}_i^j \\ \tilde{r}_i^j \end{bmatrix} + \frac{\partial \Pi(\mathbf{R}^j(r_i^j)\mathbf{P}_i + \mathbf{t}^j(r_i^j))}{\partial n_r} n_r \end{aligned} \quad (15)$$

then by substituting Eq. (15) into (14), we have

$$\mathbf{e}_i^j = \begin{bmatrix} n_c \\ n_r \end{bmatrix} - \frac{\partial \Pi(\mathbf{R}^j(r_i^j)\mathbf{P}_i + \mathbf{t}^j(r_i^j))}{\partial n_r} n_r = \mathbf{C}_i^j \begin{bmatrix} n_c \\ n_r \end{bmatrix} \quad (16)$$

recall that $[n_c \ n_r]^\top \sim \mathcal{N}(0, \mathbf{W}\Sigma\mathbf{W}^\top)$, thus \mathbf{e}_i^j follows a Gaussian distribution:

$$\mathbf{e}_i^j \sim \mathcal{N}(0, \mathbf{C}_i^j \mathbf{W} \Sigma \mathbf{W}^\top \mathbf{C}_i^{j\top}) \quad (17)$$

□

Advantages of noise covariance weighting: Note that the standardisation in Eq. (11) scaling every term by its inverse covariance matrix Σ_i^{j-1} so that all terms end up with isotropic covariance [36]. In Fig. 3, we visualize the influence of error terms standardization, which leads to two advantages:

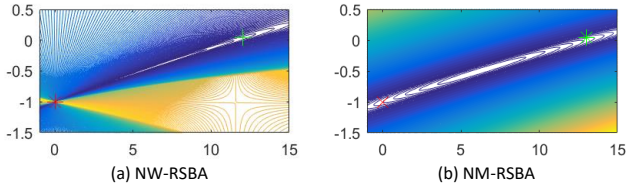


Fig. 4: The loss surfaces of (a) proposed NW-RSBA and (b) NM-RSBA [11] under the same critical configuration. The x-axis and y-axis are Y coordinate of 3D point \mathbf{P} and ω_x of camera motion respectively. The green stars are the ground truth solution (GTS) while the red stars are the degenerate solutions (DS). Notice that the path from GTS to DS in NM-RSBA is a boulevard while it is a funnel in NW-RSBA.

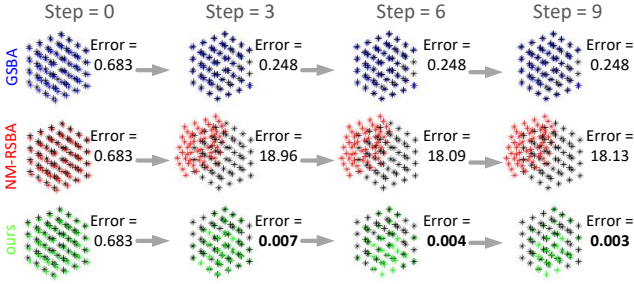


Fig. 5: Analysis of the criticality in synthetic cube scene captured by two views with parallel readout direction. GSBA provides noisy results (blue) over the ground truth (black) while NW-RSBA achieves best performance (green). In contrast, The reconstruction of NM-RSBA [11] (red) collapses to plane gradually with the BA step repeated. The detailed 3D reconstruction errors are shown beside.

- **More accurate:** With the re-weighting standardization in Eq. (11), features with a high variance which means a high probability of a large reprojection error, are offered less confidence by down-weighting their influence on the total error. A low-variance feature offers more confidence by amplifying the error terms as it is precisely localized in the image. Synthetic experiments in section. 4.1 demonstrate that noise covariance weighting significantly improves the BA accuracy under various noise levels over the NM-RSBA.
- **Handle planar degeneracy:** Note that NM-RSBA [11] recommends using images with distinct scanning directions, which strongly limits the filming manner. While C-RSBA is reported can effectively avoid the degenerate solution even using RS images with parallel scanning directions as input. Surprisingly, though the proposed NW-RSBA uses measurement-based projection, with the noise covariance weighting, it still provides stable BA results under critical configuration and even outperforms C-RSBA. As shown in Fig. 4, we interpret the improvement due to the error term standardization removing the correlation between the row index r_i^j and e_i^j . An synthetic experiment shown in Fig. 5 verifies that NM-RSBA could easily collapses into degenerate

Algorithm 3: Computation of Jacobian matrix

Input : RS camera poses $\{\mathbf{R}^j, \mathbf{t}^j, \omega^j, \mathbf{d}^j\}$, points coordinate \mathbf{P}_i and point measurement in normalized image coordinate \mathbf{q}_i^j

Output: Jacobian matrix \mathbf{J}_i^j

- 1 Calculate $\frac{\partial \hat{\mathbf{e}}_i^j}{\partial \mathbf{P}_i}$ using Eq. (32);
- 2 Calculate $\frac{\partial \hat{\mathbf{e}}_i^j}{\partial \xi^j}$ using Eq. (33);
- 3 Calculate $\frac{\partial \hat{\mathbf{e}}_i^j}{\partial \mathbf{t}^j}$ using Eq. (34);
- 4 Calculate $\frac{\partial \hat{\mathbf{e}}_i^j}{\partial \omega^j}$ using Eq. (35);
- 5 Calculate $\frac{\partial \hat{\mathbf{e}}_i^j}{\partial \mathbf{d}^j}$ using Eq. (36);
- 6 Construct $\mathbf{J}_i^j = \begin{bmatrix} \mathbf{J}_{i,rs}^j & \mathbf{J}_{i,gs}^j & \mathbf{J}_{i,p}^j \end{bmatrix} = \begin{bmatrix} [\frac{\partial \hat{\mathbf{e}}_i^j}{\partial \omega^j}, \frac{\partial \hat{\mathbf{e}}_i^j}{\partial \mathbf{d}^j}] & [\frac{\partial \hat{\mathbf{e}}_i^j}{\partial \xi^j}, \frac{\partial \hat{\mathbf{e}}_i^j}{\partial \mathbf{t}^j}] & \frac{\partial \hat{\mathbf{e}}_i^j}{\partial \mathbf{P}_i} \end{bmatrix}$;

solutions while NW-RSBA outperforms the GSBA. Note that C-RSBA claims to be able to handle such degeneracy. We found a mathematical equivalence between NW-RSBA and the normalized C-RSBA (proof in appendix. B). However, please note that C-RSBA [13] does not perform the normalization, provides analytically Jacobian and supports BA acceleration.

Jacobian of NW-RSBA: Note that BA is an iterative non-linear optimization problem basically, which can be accelerated over the numerical Jacobian searching if its analytical Jacobian of the cost function is available. Though the video-based solutions [9], [10], [33] have studied analytical Jacobian, but the Jacobian derivations of general unordered RSBA have never been addressed. Here, we introduce the derivation of the analytical Jacobian matrix of NW-RSBA.

Notice that the cost function in Eq. (11) does not follow the standard weighted least square problem because the weight is also a function of state vectors. Thus, we reformulate this question as a standard least square problem using decomposition instead of a weighted least square problem.

$$\begin{aligned} \Sigma_i^{j-1} &= (\mathbf{C}_i^j \mathbf{W} \Sigma \mathbf{W}^\top \mathbf{C}_i^{j\top})^{-1} \\ &= \mathbf{C}_i^{j-1\top} \mathbf{W}^{-\top} \Sigma^{-\frac{1}{2}} \Sigma^{-\frac{1}{2}} \mathbf{W}^{-1} \mathbf{C}_i^{j-1} \end{aligned} \quad (18)$$

substituting Eq. (18) into Eq. (11), we have

$$\begin{aligned} \theta^* &= \{\mathbf{P}^*, \mathbf{R}^*, \mathbf{t}^*, \omega^*, \mathbf{d}^*\} \\ &= \arg \min_{\theta} \sum_{j \in \mathcal{F}} \sum_{i \in \mathcal{P}_j} \mathbf{e}_i^j \Sigma_i^{j-1} \mathbf{e}_i^j \\ &= \arg \min_{\theta} \sum_{j \in \mathcal{F}} \sum_{i \in \mathcal{P}_j} \hat{\mathbf{e}}_i^j \hat{\mathbf{e}}_i^j \end{aligned} \quad (19)$$

with,

$$\hat{\mathbf{e}}_i^j = \Sigma^{-\frac{1}{2}} \mathbf{W}^{-1} \mathbf{C}_i^{j-1} \mathbf{e}_i^j \quad (19a)$$

where the new equivalent error term $\hat{\mathbf{e}}_i^j$ follows the standard least square problem, then we can derive the analytical Jacobian matrix of Eq. (19) by using the chain rule (details in appendix. A). Notice that we use $\xi_i^j \in \mathfrak{so}(3)$ to



Fig. 6: Example Jacobian matrices with 3 points and 2 cameras in (a) GSBA, RSBA with (b) series connection, and (c) parallel connection.

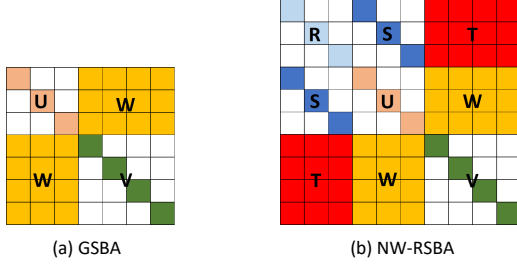


Fig. 7: Example approximate Hessian matrices with 4 points and 3 cameras in (a) GSBA and (b) proposed NW-RSBA.

parameterize $\mathbf{R}_i^j \in \mathbb{SO}(3)$ as $\mathbf{R}_i^j = \mathbf{Exp}(\xi_i^j)$ in whole optimization, so the update scheme is also in $\mathbb{SO}(3)$ as $\theta_R^* = \mathbf{Log}(\mathbf{Exp}(\delta_R) \times \mathbf{Exp}(\theta_R))$. \mathbf{Exp} and \mathbf{Log} defined in Eq. (29) represent the mapping operator and inverse mapping operator between lie group $\mathbb{SO}(3)$ and lie algebra $\mathfrak{so}(3)$.

In summary, we first construct the re-weighted error using Alg. 2 and then compute the Jacobian of NW-RSBA following Alg. 3.

3.3 NW-RSBA Acceleration

Based on the sparsity structure (Fig. 6(a)) of the Jacobian matrix, the marginalization [36], [37] technique using the Schur complement has achieved significant success in speeding up the GSBA problem. However, the acceleration strategy has never been addressed for the general unordered RSBA in [11], [13], [33]. As shown in Fig. 6(b)(c), we organize the RSBA Jacobian matrices in two styles, namely series connection and parallel connection.

- **Series connection:** By regarding camera pose and instantaneous-motion in Jacobian matrix (Fig. 6(b)) as an entirety, we can simply use the **one-stage Schur complement** technique [37] to marginalize out the 3D point and compute the update state vector for $\mathbf{R}, \mathbf{t}, \omega, \mathbf{d}$ first, followed by back substitution for update state vector of points.

- **Parallel connection:** Due to the dependencies between camera pose and instantaneous-motion in the Jacobian matrix (Fig. 6(c)), we propose a **two-stage Schur complement** strategy to speed up the RSBA. When solving the non-linear least square problem (e.g. Gauss-Newton), the approximate Hessian matrix for Eq. (19) is defined as

Algorithm 4: Solve the normal equation (26) using two-stage Schur complement

Input : Jacobian matrix \mathbf{J} and weighted error vector $\hat{\mathbf{e}}$

Output: Updated vector δ

- 1 Compute Schur complement matrix \mathbf{S}_p and \mathbf{S}_{rs} using Eq. (22) and (23);
- 2 Compute auxiliary vectors \mathbf{t}^* and \mathbf{u}^* using Eq. (25) and (24);
- 3 Solve Eq. (26) cascadingly:
 - Get δ_{rs} by solving $\mathbf{S}_{rs}\delta_{rs} = -\mathbf{t}^*$;
 - Get δ_{gs} by solving $\mathbf{U}^*\delta_{gs} = -\mathbf{u}^* - \mathbf{S}^{*\top}\delta_{rs}$;
 - Get δ_p by solving $\mathbf{V}\delta_p = -\mathbf{v} - \mathbf{T}^\top\delta_{rs} - \mathbf{W}^\top\delta_{gs}$;
 - Stack $\delta_{gs}, \delta_{rs}, \delta_p$ into δ ;

$$\mathbf{J}^\top \mathbf{J} = \begin{bmatrix} \mathbf{J}_{rs}^\top \mathbf{J}_{rs} & \mathbf{J}_{rs}^\top \mathbf{J}_{gs} & \mathbf{J}_{rs}^\top \mathbf{J}_p \\ \mathbf{J}_{gs}^\top \mathbf{J}_{rs} & \mathbf{J}_{gs}^\top \mathbf{J}_{gs} & \mathbf{J}_{gs}^\top \mathbf{J}_p \\ \mathbf{J}_p^\top \mathbf{J}_{rs} & \mathbf{J}_p^\top \mathbf{J}_{gs} & \mathbf{J}_p^\top \mathbf{J}_p \end{bmatrix} = \begin{bmatrix} \mathbf{R} & \mathbf{S} & \mathbf{T} \\ \mathbf{S}^\top & \mathbf{U} & \mathbf{W} \\ \mathbf{T}^\top & \mathbf{W}^\top & \mathbf{V} \end{bmatrix} \quad (20)$$

with,

$$\mathbf{J} = [\mathbf{J}_{rs} \quad \mathbf{J}_{gs} \quad \mathbf{J}_p] = \begin{bmatrix} \frac{\partial \hat{\mathbf{e}}}{\partial \mathbf{x}_{rs}} & \frac{\partial \hat{\mathbf{e}}}{\partial \mathbf{x}_{gs}} & \frac{\partial \hat{\mathbf{e}}}{\partial \mathbf{x}_p} \end{bmatrix} \quad (20a)$$

$$\hat{\mathbf{e}} = \begin{bmatrix} \{\hat{\mathbf{e}}_i^j\} \end{bmatrix}, \quad \mathbf{x}_{gs} = \begin{bmatrix} \{\mathbf{R}_i^j\} & \{\mathbf{t}_i^j\} \end{bmatrix}, \quad (20b-1)$$

$$\mathbf{x}_{rs} = \begin{bmatrix} \{\omega_i^j\} & \{\mathbf{d}_i^j\} \end{bmatrix}, \quad \mathbf{x}_p = \begin{bmatrix} \{\mathbf{P}_i\} \end{bmatrix} \quad (20b-2)$$

where, $\hat{\mathbf{e}}_i^j$ is a error term defined in Eq. (19) for $j^{\text{th}}, j \in \mathcal{F}$ camera and 3D point $\mathbf{P}_i, i \in \mathcal{P}_j$. $\mathbf{R}, \mathbf{U}, \mathbf{V}, \mathbf{S}, \mathbf{T}$ and \mathbf{W} are submatrices computed by the derivations $\mathbf{J}_{rs}, \mathbf{J}_{gs}$ and \mathbf{J}_p .

As shown in Alg. 4, based on the analytical Hessian approximate matrix in Eq. (20), the two-stage Schur complement strategy consists of 3 steps:

▷ **Step 1: Construct normal equation.** In each iteration, using this form of the Jacobian and corresponding parameter vectors and the error vector, the normal equation follows

$$\mathbf{J}^\top \mathbf{J} \delta = \begin{bmatrix} \mathbf{R} & \mathbf{S} & \mathbf{T} \\ \mathbf{S}^\top & \mathbf{U} & \mathbf{W} \\ \mathbf{T}^\top & \mathbf{W}^\top & \mathbf{V} \end{bmatrix} \begin{bmatrix} \delta_{rs} \\ \delta_{gs} \\ \delta_p \end{bmatrix} = -\mathbf{J}^\top \hat{\mathbf{e}} = - \begin{bmatrix} \mathbf{t} \\ \mathbf{u} \\ \mathbf{v} \end{bmatrix} \quad (21)$$

where δ_{gs}, δ_{rs} and δ_p are the updating vectors to $\mathbf{x}_{gs}, \mathbf{x}_{rs}$ and \mathbf{x}_p , while \mathbf{t}, \mathbf{u} , and \mathbf{v} are the corresponding descent direction. Such formed normal equations show a block sparsity, suggesting that we can efficiently compute it.

▷ **Step 2: Construct Schur complement.** Different from the one-stage Schur complement in GSBA, we construct two-stage Schur complements $\mathbf{S}_p, \mathbf{S}_{rs}$ and two auxiliary vectors \mathbf{u}^* and \mathbf{t}^* to Eq. (21) as

$$\mathbf{S}_p = \begin{bmatrix} \mathbf{R}^* & \mathbf{S}^* \\ \mathbf{S}^{*\top} & \mathbf{U}^* \end{bmatrix} = \begin{bmatrix} \mathbf{R} - \mathbf{T}\mathbf{V}^{-1}\mathbf{T}^\top & \mathbf{S} - \mathbf{T}\mathbf{V}^{-1}\mathbf{W}^\top \\ \mathbf{S}^\top - \mathbf{W}\mathbf{V}^{-1}\mathbf{T}^\top & \mathbf{U} - \mathbf{W}\mathbf{V}^{-1}\mathbf{W}^\top \end{bmatrix} \quad (22)$$

$$\mathbf{S}_{rs} = \mathbf{R}^* - \mathbf{S}^* \mathbf{U}^{*-1} \mathbf{S}^{*\top} \quad (23)$$

$$\mathbf{u}^* = \mathbf{u} - \mathbf{W}\mathbf{V}^{-1}\mathbf{v} \quad (24)$$

$$\mathbf{t}^* = \mathbf{t} - \mathbf{T}\mathbf{V}^{-1}\mathbf{v} - \mathbf{S}^* \mathbf{U}^{*-1} \mathbf{u}^* \quad (25)$$

▷ **Step 3: Orderly solve δ_{gs} , δ_{rs} and δ_p .** Based on \mathbf{S}_p , \mathbf{S}_{rs} , \mathbf{u}^* and \mathbf{t}^* , we reformulate the normal equation as

$$\begin{bmatrix} \mathbf{S}_{rs} & \mathbf{0} & \mathbf{0} \\ \mathbf{S}^{*\top} & \mathbf{U}^* & \mathbf{0} \\ \mathbf{T}^\top & \mathbf{W}^\top & \mathbf{V} \end{bmatrix} \begin{bmatrix} \delta_{rs} \\ \delta_{gs} \\ \delta_p \end{bmatrix} = - \begin{bmatrix} \mathbf{t}^* \\ \mathbf{u}^* \\ \mathbf{v} \end{bmatrix} \quad (26)$$

which enables us to compute δ_{rs} first, and then back substitutes the results to get δ_{gs} . Finally, we can obtain δ_p based on the 3rd row of Eq. (26).

3.4 Implementation

In summary, we follow the pipeline described in Alg. 1 to implement the proposed *NW-RSBA* in C++ using typical non-linear least square solver (e.g. G2O [38]) for the sparse BA optimization in Eq. (19) with analytical Jacobian and two-stage Schur complement acceleration in section. 3.3. It is important to note that existing video-based RSBA methods cannot be applied to various SfM and SLAM solutions. In contrast, the implemented *NW-RSBA* can serve as a little module and can be easily plug-in such context:

- **RS-SfM:** VisualSfM [3] is a successful incremental SfM solution. We augment the original VisualSfM to handle the unordered images with RS effect as input by shifting the incremental GSBA pipeline with the proposed *NW-RSBA*.
- **RS-SLAM:** Orb-SLAM [15] is a stable SLAM solution for Monocular camera. We augment the original version of Orb-SLAM to handle RS input by simply replacing the local BA and full BA modules with the proposed *NW-RSBA*.

4 EXPERIMENTAL EVALUATION

In our experiments, the proposed method is compared to three state-of-the-art unordered RSBA solutions:

- *GSBA*: SBA [37].
- *DC-RSBA*: direct camera-based RSBA [13].
- *DM-RSBA*: direct measurement-based RSBA [33].
- *NM-RSBA*: normalized measurement-based RSBA [11].
- *NW-RSBA*: proposed normalized weighted RSBA.

4.1 Synthetic Data

• **Setting** We simulate 5 RS cameras located randomly on a sphere with a radius of 20 units pointing to a cubical scene with 56 points. The RS image size is 1280×1080 px, the focal length is about 1000, and the optical centre is at the centre of the image domain. We compare all methods by varying the speed, the noise on image measurements, and the readout direction. The results are obtained after collecting the errors over 300 trials each epoch. The default setting is 10 degs/frame and 1 unit/frame for angular and linear velocity, standard covariance noise.

• **Metrics** We measure the reconstruction errors (mean difference between computed and ground truth 3D points) and pose errors (mean difference between the computed and ground truth rotation $\mathbf{e}_{\text{rot}} = \arccos((\text{tr}(\mathbf{R}\mathbf{R}_{\text{GT}}^\top) - 1)/2)$ and translation $\mathbf{e}_{\text{trans}} = \arccos(\mathbf{t}^\top \mathbf{t}_{\text{GT}} / (\|\mathbf{t}\| \|\mathbf{t}_{\text{GT}}\|))$ of each camera in deg).

Varying Speed. We evaluate the accuracy of five approaches against increasing angular and linear velocity from 0 to

20 degs/frame and 2 units/frame gradually, but with random directions. The results in Fig. 8(a)(b)(c) show that the estimated errors of *GSBA* grow with speed while *DC-RSBA* and *DM-RSBA* provides significant better estimation. *NM-RSBA* achieves better results with slow kinematics, while its errors grow dramatically beyond 10 degs/frame and 1 units/s. In contrast, the proposed *NW-RSBA* provides the best results under all configurations.

Varying Noise Level. In Fig. 8(d)(e)(f), when noise raises from 0 to 2 pixels, the errors of all approaches grow linearly. However, *GSBA* shows better robustness to noise than all the rest RS methods, even though its global performance is terrible. In all cases, the proposed method *NW-RSBA* achieves the best performance with all noise levels.

Varying Readout Direction. We evaluate the robustness of five methods with an RS critical configuration, namely, the readout directions of all views are almost parallel. Thus, we vary the readout directions of the cameras from parallel to perpendicular by increasing the angle between them from 0 deg to 90 degs. In Fig. 8(g)(h)(i), we observe that all four RSBA methods outperform *GSBA* with angle larger than 50 degs. While the angle becomes smaller, the reconstruction error of *DM-RSBA*, *DC-RSBA* and *DM-RSBA* grow dramatically, which means that they collapse into the planar degenerated solution. In contrast, the proposed *NW-RSBA* provides stable results under all settings, even with the parallel readout direction.

Runtime. We compare the time cost of all methods. As shown in Fig. 9 that without analytical Jacobian, *DC-RSBA* provides the slowest performance while the proposed *NW-RSBA* achieves similar efficiency as *NM-RSBA*. However, by using Schur complement strategies, *NM-RSBA-1S* and *NM-RSBA-2S* reduce the runtime. Note that *NM-RSBA-2S* uses the proposed two-stage Schur complement to the Jacobian matrices with parallel connection achieves an order of magnitude faster than *NM-RSBA*. The results also prove that *NM-RSBA* is slower than *GSBA* mainly because of massive Jacobian matrix construction, by a factor roughly around 6.

4.2 Real Data

Datasets. We compare all the RSC methods in the following publicly available RS datasets:

- **WHU-RSVI:** WHU dataset¹ was published in [39] and provided ground truth synthetic GS images, RS images and camera poses.
- **TUM-RSVI:** The TUM RS dataset² was published in [14] and contained time-synchronized global-shutter, and rolling-shutter images captured by a non-perspective camera rig and ground-truth poses recorded by motion capture system for ten RS video sequences.

1. <http://aric.whu.edu.cn/caolike/2019/11/05/the-whu-rsvi-dataset/>

2. <https://vision.in.tum.de/data/datasets/rolling-shutter-dataset>

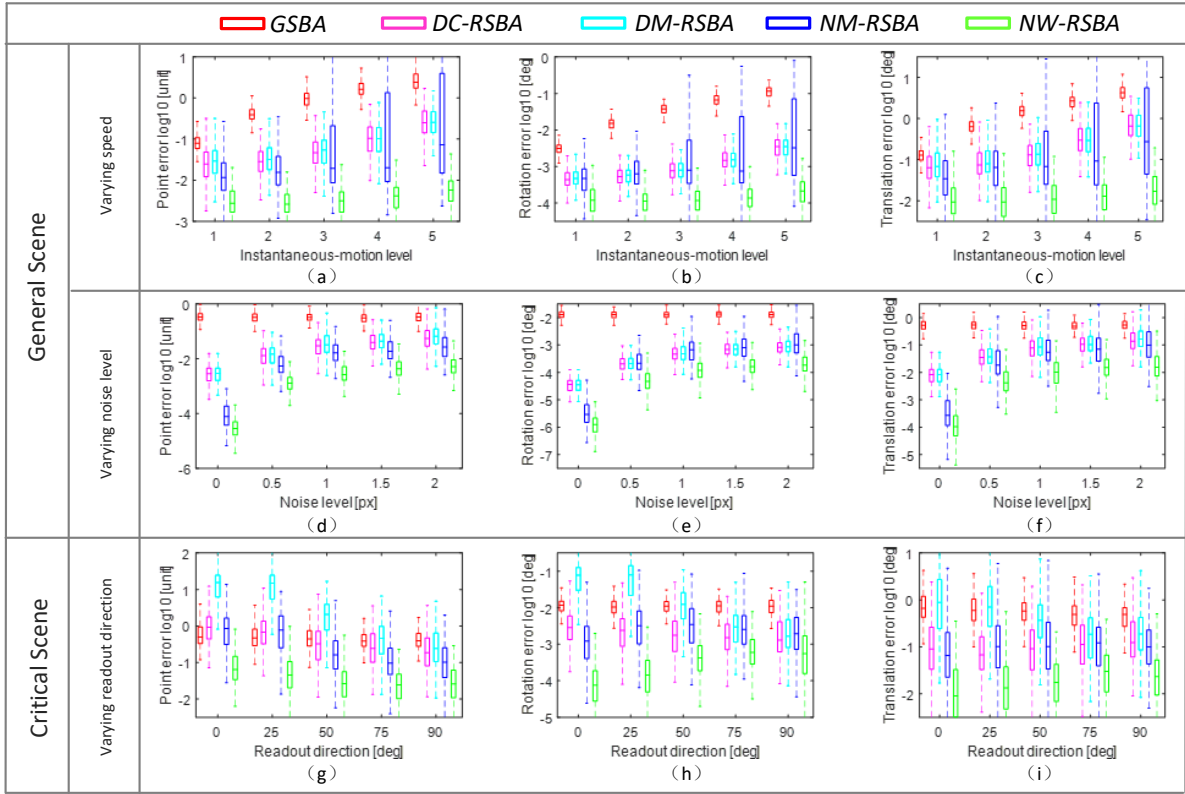


Fig. 8: Camera pose (2nd and 3rd columns) and reconstruction (1st column) errors of *GSBA*, *DC-RSBA*, *DM-RSBA*, *NM-RSBA* and *NW-RSBA* with increasing angular and linear velocity (1st row) and noise levels in image (2nd row) in general scene, also with increasing readout directions in critical scene (3rd row).

Evaluation metrics. In this section, we use three metrics to evaluate the performances, namely absolute trajectory error, tracking duration and real-time factor.

- **Absolute trajectory error (ATE).** We use the absolute trajectory error (*ATE*) [14] to evaluate the VO results quantitatively. Given ground truth frame positions $\bar{\mathbf{c}}_i \in \mathbb{R}^3$ and corresponding *Orb-SLAM* [15] tracking results $\mathbf{c}_i \in \mathbb{R}^3$ using corrected sequence by each RSC method. It is defined as

$$e_{ate} = \min_{\mathbf{T} \in \text{Sim}(3)} \sqrt{\frac{1}{n} \sum_{i=1}^n \|\mathbf{T}(\mathbf{c}_i) - \bar{\mathbf{c}}_i\|^2} \quad (27)$$

where $\mathbf{T} \in \text{Sim}(3)$ is a similarity transformation that aligns the estimated trajectory with the ground truth one since the scale is not observable for monocular methods. We run each method 20 times on each sequence to obtain the ATE e_{ate} .

- **Tracking duration (DUR).** Besides, we find out that some RSC solutions provide the results of corrections that are even worse than the original input RS frames. This leads to failure in tracking and makes *Orb-SLAM* interrupt before the latest capture frame. Therefore, we use the ratio of the successfully tracked frames out of the total frames *DUR* as an evaluation metric.
- **Realtime factor ϵ .** The realtime factor ϵ is calculated as the sequence's actual duration divided by the algo-

TABLE 2: Statistics of 10 sequences from TUM-RSVI [14] and 2 sequences from WHU-RSVI [39] datasets. The realtime factors of conventional *Orb-SLAM*, *Orb-SLAM*+*NM-RSBA* [11], and proposed *Orb-SLAM*+*NW-RSBA* are given by ϵ .

Seq	Duration [s]	length [m]	Realtime factor $\epsilon \uparrow$		
			<i>Orb-SLAM</i> [15]	<i>Orb-SLAM</i> + <i>NM-RSBA</i> [11]	<i>Orb-SLAM</i> + <i>NW-RSBA</i>
#1	40	46	1.47	1.48	1.38
#2	27	37	1.51	1.40	1.40
#3	50	44	1.47	1.41	1.39
#4	38	30	1.61	1.35	1.56
#5	85	57	1.51	1.28	1.38
#6	43	51	1.47	1.37	1.38
#7	39	45	1.61	1.47	1.49
#8	53	46	1.56	1.37	1.35
#9	45	46	1.61	1.51	1.55
#10	54	41	1.56	1.46	1.47
t1-fast	28	50	1.92	1.51	1.81
t2-fast	29	53	1.92	1.40	1.67

rithm's processing time.

4.2.1 RSSLAM

In the application of SLAM, we compare the performance of conventional GS based *Orb-SLAM* [15] versus augmented versions with proposed *NW-RSBA* and *NM-RSBA* [11] on 12 RS sequences (around 8 min and 578 m traversed distance). Table. 2 shows some statistics of the individual sequences. Note that we did not compare *DC-RSBA* [13] and *DM-RSBA* [33] in this experiment since their supplied analytical Jacobian matrices are unavailable

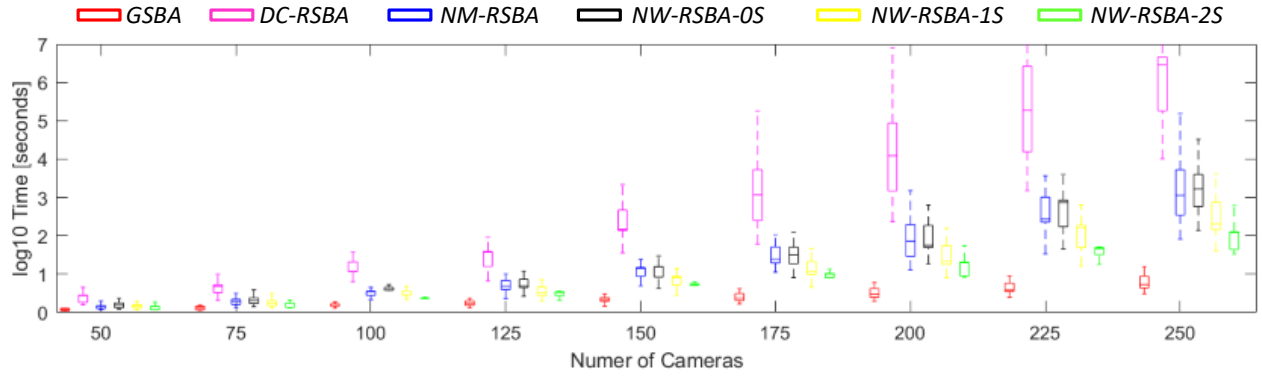


Fig. 9: Time cost of *GSBA* [37], *DC-RSBA* [13], *NM-RSBA* [11], *NW-RSBA-0S* (without Schur complement), *NW-RSBA-1S* (one-stage Schur complement to Jacobian matrices with series connection), and proposed *NW-RSBA-2S* (two-stage Schur complement to Jacobian matrices with parallel connection) with increasing camera number.

TABLE 3: Ratio of successful tracked frames divided by of the total frames *DUR* of orb-SLAM [15] augmented by different RSBA methods. Best results are shown in green.

Input	Methods	DUR↑											
		TUM-RSVI [14]										WHU-RSVI [39]	
		#1	#2	#3	#4	#5	#6	#7	#8	#9	#10	t1-fast	t2-fast
GS data	Orb-SLAM [15]	1	1	1	1	1	1	1	1	1	1	1	1
RS data	Orb-SLAM [15]	0.50	0.90	0.58	1	1	0.76	0.89	0.79	0.14	0.29	1	1
	Orb-SLAM+NM-RSBA [11]	0.28	0.81	0.36	1	1	0.76	0.97	0.96	0.23	0.29	1	1
	Orb-SLAM+NW-RSBA (ours)	1	1	1	1	1	1	1	1	0.42	1	1	1

TABLE 4: Absolute trajectory error (ATE) of different RSC methods after Sim(3) alignment to ground truth. Best results is shown in green. Since some methods will lose tracking without processing the whole frame, thus we highlight the background of each cell with different colours depending on its corresponding *DUR* value. Specifically, $DUR > 0.9$, $0.5 < DUR \leq 0.9$ and $DUR \leq 0.5$ are highlighted in light green, cyan, and orange.

Input	Methods	ATE↓											
		TUM-RSVI [14]										WHU-RSVI [39]	
		#1	#2	#3	#4	#5	#6	#7	#8	#9	#10	t1-fast	t2-fast
GS data	Orb-SLAM [15]	0.015	0.013	0.018	0.107	0.030	0.013	0.054	0.053	0.020	0.024	0.044	0.008
RS data	Orb-SLAM [15]	0.059	0.100	0.411	0.126	0.055	0.044	0.217	0.218	0.176	0.373	0.237	0.018
	Orb-SLAM+NM-RSBA [11]	0.115	0.088	0.348	0.120	0.062	0.060	0.251	0.246	0.156	0.307	0.204	0.030
	Orb-SLAM+NW-RSBA (ours)	0.011	0.008	0.031	0.071	0.034	0.008	0.260	0.115	0.028	0.108	0.054	0.012

and thus leads to a vast time-consuming result.

Tracking duration. As shown in Fig. 3, all methods successfully track all frames in the WHU-RSVI dataset with $DUR = 1$. However, conventional *Orb-SLAM* and *Orb-SLAM+NM-RSBA* [11] fail with an average $DUR < 0.5$ in most sequences from the TUM-RSVI dataset when the camera moves fast. The poor 3D reconstruction and camera pose estimation of *Orb-SLAM* and *Orb-SLAM+NM-RSBA* raises the mistracking issue in the preceding frames. Hence the tracking of the later frames will lose, and the following 2D-3D registration will become unfeasible. In contrast, the proposed *Orb-SLAM+NW-RSBA* achieves completed tracking with $DUR = 1$ in almost all sequences from WHU-RSVI and TUM-RSVI datasets.

Absolute trajectory error. The SLAM results on WHU-RSVI and TUM-RSVI datasets demonstrate that the proposed *Orb-SLAM+NW-RSBA* is superior to *Orb-SLAM* and *Orb-SLAM+NM-RSBA* when dealing with RS effect. Qualitatively, this is clearly visible in Figs. 1 and 10. The sparse 3D reconstructions look much cleaner for *Orb-SLAM+NW-RSBA* and close to the ground truth, while *Orb-SLAM* and *Orb-SLAM+NM-RSBA* produce inconsistent and noise edges when revisiting a section of the room. More significant is the large systematic drift of the camera trajectories. The quantitative difference also becomes apparent in table. 4. *Orb-SLAM+NW-RSBA* outperforms *Orb-SLAM* and *Orb-SLAM+NM-RSBA* both in terms of accuracy and stability.

Real-time factor. Table. 2 shows statistics about the 12 se-

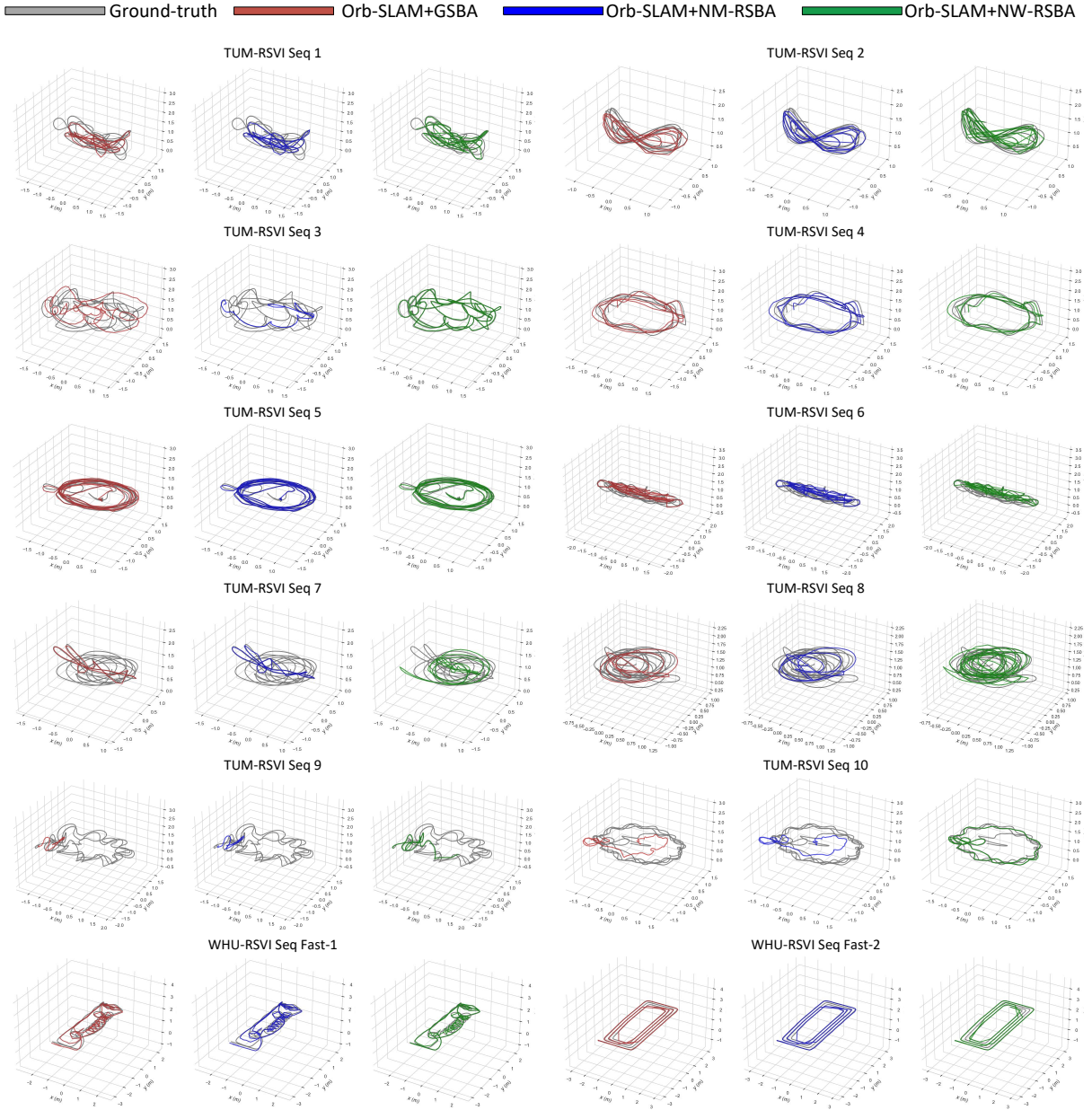


Fig. 10: Ground truth and trajectories estimated by GSBA [37], NM-RSBA [11] and proposed NW-RSBA after Sim(3) alignment on 10 sequences from TUM-RSVI [14] and 2 sequences from WHU-RSVI [39] datasets.

quences and the performance of three approaches run on an AMD Ryzen 7 5800H CPU. The results verify that all three methods achieve real-time performance with $\epsilon > 1$. One can also confirm that the proposed *Orb-SLAM+NW-RSBA* is slower than conventional *Orb-SLAM* by a factor roughly around 1.2 but is slightly faster than *Orb-SLAM+NM-RSBA*.

4.2.2 Quantitative Ablation Study

We randomly choose 8 frames from each of 12 RS sequences to generate 12 unordered SfM datasets and evaluate the RSBA performance via average ATE and runtime. Besides, we ablate the proposed NW-RSBA and compare quantitatively with related approaches. The results are presented in table. 5.

TABLE 5: Quantitative ablation study of RSSfM on TUM-RSVI [14] and WHU-RSVI [39] datasets. ATE: absolute trajectory error of estimated camera pose in meter (m), Runtime: time cost in seconds. Best and second best results are shown in green and blue respectively.

Ablation	Approach	ATE (m)	Runtime (s)
	GSBA [37]	0.210	2.9
	DC-RSBA [13]	0.016	1302
No normalization & weighting	DM-RSBA [33]	0.023	740
No weighting	NM-RSBA [11]	0.020	15.8
No normalization	W-RSBA	0.013	16.1
No Schur complement	NW-RSBA-0S		16.9
with 1-stage Schur complement	NW-RSBA-1S	0.007	13.0
Consolidated	NW-RSBA-2S		9.8

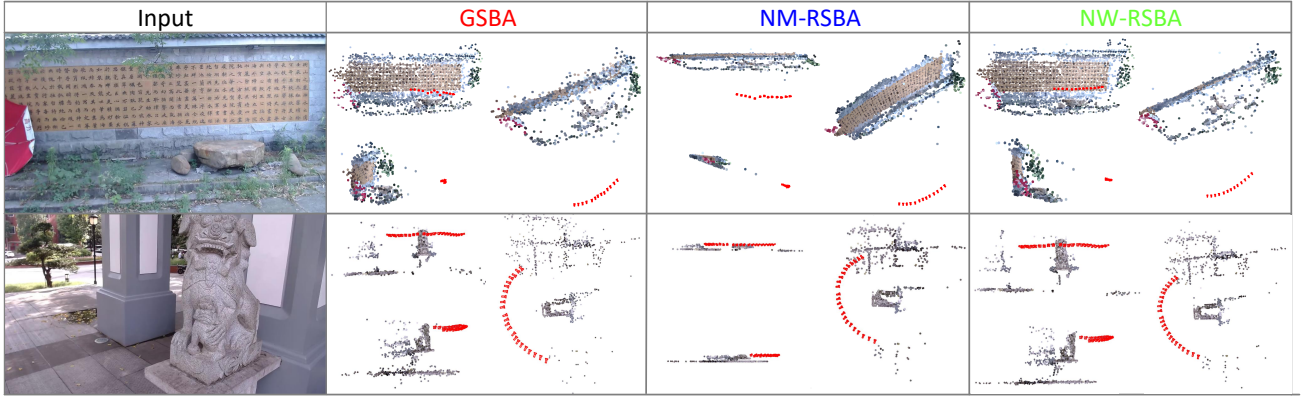


Fig. 11: Three-view graph of reconstructions using SfM pipeline using *GSBA* [37], *NM-RSBA* [11] and proposed *NW-RSBA*.

Comparison with existing baselines. We compute the performance of the baseline methods *GSBA* [37], *DC-RSBA* [13], *DM-RSBA* [33] and *NM-RSBA* [11]. *NW-RSBA* obtains ATE of 0.007 which is half of second best method *DC-RSBA* and nearly 3% of *GSBA*.

Normalization vs. Direct measurement. The removal of normalization from proposed *NW-RSBA* adversely increases ATE up to 100%. Interestingly, removing the normalization in *NM-RSBA* [11] also leads to 15% growth in ATE. This further accentuates the value of using normalized measurements over direct ones.

Covariance weighting. The removal of covariance weighting from proposed *NW-RSBA* adversely impacts the quality of camera pose estimation. The growth from 0.007 to 0.020 is observed for the ATE. We believe that covariance weighting helps BA leverage the RS effect and random image noise better.

Schur Complement Acceleration. We ablate the consolidated version *NW-RSBA-2S* to *NW-RSBA-0S* by removing the proposed 2-stage Schur complement strategy and compare to *NW-RSBA-1S* which uses 1-stage Schur complement as well. The increases from 9.8s to 13.0s and 16.9s is observed for average runtime. Despite the fact *NW-RSBA-2S* is slower than *GSBA* by a factor of 3, the proposed solution is 2 times faster than *NM-RSBA*, 2 orders of magnitude faster than *DC-RSBA* and *DM-RSBA*.

4.2.3 Qualitative Samples of RSSfM

We captured two datasets using a smartphone camera and kept the readout direction vertically. Note that such setting is a critical configuration in RSBA and will quickly lead to a planar degenerated solution for *NM-RSBA* [11]. An incremental SfM pipeline similar to [3] was used to provide a baseline reconstruction.

NW-RSBA vs. GSBA. As shown in Fig. 11 that our methods work better in motion and 3D scene estimation while *GSBA* [37] obtains a deformed reconstruction. Specifically, the sparse 3D reconstructions look much cleaner for *NW-RSBA*, while *GSBA* provides rough surfaces.

Besides, the estimated camera trajectories are more clean and smooth.

NW-RSBA vs. NM-RSBA. As shown in Fig. 11 that *NM-RSBA* reconstructs 3D scenes which collapse into a plane since the datasets contain only one readout direction. In contrast, the proposed *NW-RSBA* provide correct reconstructions. The results also verify our discussion in section. 3.2 that using error covariance weighting can avoid the planar degenerate solution.

5 CONCLUSION

This paper presents a novel RSBA solution without any assumption on camera image manner, additional sensors, and type of measurement input. We explain the importance of conducting normalization and present a weighting technique in RSBA, which leads to normalized weighted RSBA. Extensive experiments in real and synthetic data verify the effectiveness and efficiency of the proposed *NW-RSBA* method. To the best of our knowledge, this is the first RSBA method to handle common planar degeneracy. Besides, we also demonstrate that the proposed RSBA algorithm can be easily applied to existing GS-based SfM and SLAM frameworks.

REFERENCES

- [1] R. Hartley and A. Zisserman, *Multiple view geometry in computer vision*. Cambridge university press, 2003.
- [2] N. Snavely, S. M. Seitz, and R. Szeliski, "Photo tourism: exploring photo collections in 3d," in *Siggraph*, 2006.
- [3] C. Wu et al., "Visualsfm: A visual structure from motion system," 2011.
- [4] G. Klein and D. Murray, "Parallel tracking and mapping on a camera phone," in *ISMAR*, 2009.
- [5] K. Yousif, A. Bab-Hadiashar, and R. Hoseinnezhad, "An overview to visual odometry and visual slam: Applications to mobile robotics," *Intelligent Industrial Systems*, 2015.
- [6] M. Meingast, C. Geyer, and S. Sastry, "Geometric models of rolling-shutter cameras," in *OMNIVIS*, 2005.
- [7] C. Albl, Z. Kukelova, V. Larsson, and T. Pajdla, "Rolling shutter camera absolute pose," *PAMI*, 2019.
- [8] Y. Dai, H. Li, and L. Kneip, "Rolling shutter camera relative pose: generalized epipolar geometry," in *CVPR*, 2016.
- [9] J. Hedborg, P.-E. Forssen, M. Felsberg, and E. Ringaby, "Rolling shutter bundle adjustment," in *CVPR*, 2012.

- [10] S. Im, H. Ha, G. Choe, H.-G. Jeon, K. Joo, and I. S. Kweon, "Accurate 3d reconstruction from small motion clip for rolling shutter cameras," *PAMI*, 2018.
- [11] C. Albl, A. Sugimoto, and T. Pajdla, "Degeneracies in rolling shutter sfm," in *ECCV*, 2016.
- [12] E. Ito and T. Okatani, "Self-calibration-based approach to critical motion sequences of rolling-shutter structure from motion," in *CVPR*, 2016.
- [13] Y. Lao, O. Ait-Aider, and H. Araujo, "Robustified structure from motion with rolling-shutter camera using straightness constraint," *Pattern Recognition Letters*, 2018.
- [14] D. Schubert, N. Demmel, L. von Stumberg, V. Usenko, and D. Cremers, "Rolling-shutter modelling for direct visual-inertial odometry," in *IROS*, 2019.
- [15] R. Mur-Artal, J. M. M. Montiel, and J. D. Tardos, "Orb-slam: a versatile and accurate monocular slam system," *T-RO*, 2015.
- [16] J. Hedborg, E. Ringaby, P.-E. Forssén, and M. Felsberg, "Structure and motion estimation from rolling shutter video," in *ICCV Workshops*, 2011.
- [17] B. Zhuang, L.-F. Cheong, and G. H. Lee, "Rolling-shutter-aware differential sfm and image rectification," in *ICCV*, 2017.
- [18] A. Patron-Perez, S. Lovegrove, and G. Sibley, "A spline-based trajectory representation for sensor fusion and rolling shutter cameras," *IJCV*, 2015.
- [19] L. Oth, P. Furgale, L. Kneip, and R. Siegwart, "Rolling shutter camera calibration," in *Proceedings of the IEEE Conference on Computer Vision and Pattern Recognition*, 2013, pp. 1360–1367.
- [20] M. Li, B. H. Kim, and A. I. Mourikis, "Real-time motion tracking on a cellphone using inertial sensing and a rolling-shutter camera," in *ICRA*, 2013.
- [21] B. Klingner, D. Martin, and J. Roseborough, "Street view motion-from-structure-from-motion," in *ICCV*, 2013.
- [22] O. Saurer, M. Pollefeys, and G. Hee Lee, "Sparse to dense 3d reconstruction from rolling shutter images," in *CVPR*, June 2016.
- [23] H. Ovrén and P.-E. Forssén, "Spline error weighting for robust visual-inertial fusion," in *CVPR*, 2018.
- [24] O. Ait-Aider and F. Berry, "Structure and kinematics triangulation with a rolling shutter stereo rig," in *ICCV*, 2009.
- [25] O. Saurer, K. Koser, J.-Y. Bouguet, and M. Pollefeys, "Rolling shutter stereo," in *ICCV*, 2013.
- [26] Y. Lao, O. Ait-Aider, and A. Bartoli, "Solving rolling shutter 3d vision problems using analogies with non-rigidity," *IJCV*, 2021.
- [27] J. Engel, V. Koltun, and D. Cremers, "Direct sparse odometry," *PAMI*, 2017.
- [28] J. Engel, T. Schöps, and D. Cremers, "Lsd-slam: Large-scale direct monocular slam," in *ECCV*, 2014.
- [29] J. H. Kim, C. Cadena, and I. Reid, "Direct semi-dense slam for rolling shutter cameras," in *ICRA*, 2016.
- [30] D. Schubert, N. Demmel, V. Usenko, J. Stückler, and D. Cremers, "Direct sparse odometry with rolling shutter," *ECCV*, 2018.
- [31] J. Engel, V. Usenko, and D. Cremers, "A photometrically calibrated benchmark for monocular visual odometry," *arXiv preprint*, 2016.
- [32] L. Magerand, A. Bartoli, O. Ait-Aider, and D. Pizarro, "Global optimization of object pose and motion from a single rolling shutter image with automatic 2d-3d matching," in *ECCV*, 2012.
- [33] G. Duchamp, O. Ait-Aider, E. Royer, and J.-M. Lavest, "A rolling shutter compliant method for localisation and reconstruction," in *VISAPP*, 2015.
- [34] V. Rengarajan, A. N. Rajagopalan, and R. Aravind, "From bows to arrows: Rolling shutter rectification of urban scenes," in *CVPR*, 2016.
- [35] P. Purkait, C. Zach, and A. Leonardis, "Rolling shutter correction in manhattan world," in *ICCV*, 2017, pp. 882–890.
- [36] B. Triggs, P. F. McLauchlan, R. I. Hartley, and A. W. Fitzgibbon, "Bundle adjustment—a modern synthesis," in *International workshop on vision algorithms*. Springer, 1999, pp. 298–372.
- [37] M. I. Lourakis and A. A. Argyros, "Sba: A software package for generic sparse bundle adjustment," *ACM Transactions on Mathematical Software (TOMS)*, vol. 36, no. 1, pp. 1–30, 2009.
- [38] G. Grisetti, R. Kümmerle, H. Strasdat, and K. Konolige, "g2o: A general framework for (hyper) graph optimization," in *Proceedings of the IEEE international conference on robotics and automation (ICRA)*, Shanghai, China, 2011, pp. 9–13.
- [39] L. Cao, J. Ling, and X. Xiao, "The whu rolling shutter visual-inertial dataset," *IEEE Access*, vol. 8, pp. 50 771–50 779, 2020.
- [40] C. Forster, L. Carlone, F. Dellaert, and D. Scaramuzza, "On-manifold preintegration for real-time visual-inertial odometry," *IEEE Transactions on Robotics*, vol. 33, no. 1, pp. 1–21, 2016.



Bangyan Liao is pursuing his Bachelor's degree in Electrical and Information Engineering from Hunan University. He is also a member of the NAIL research group since 2021 headed by Professor Yi Zhou at Hunan University. His research interests include visual odometry/simultaneous localization and mapping, optimization problems in computer vision, Rolling Shutter cameras, and Dynamic Vision Sensors.



Delin Qu received the Bachelor's degree in the College of Computer Science and Electronic Engineering from Hunan University. Currently, he is pursuing his PhD degree in computer vision at School of Computer Science, Fudan University and interning as a researcher in Shanghai AI Lab. His research interests are in the area of computer vision and computational imaging.



Yifei Xue received the M.Sc degree in surveying and mapping from the State Key Laboratory of Information Engineering in Surveying, Mapping, and Remote Sensing (LIESMARS), Wuhan University, China, in 2014. He is currently the Director of the Postdoctoral Innovation Practice Base of Jiangxi Provincial Natural Resources Cause Development Center. His research interests focus on satellite imagery processing, computational photography, and machine learning.



Huiqin Zhang is a master's candidate at Hunan University, where she works in Computational Photography and Computer Vision. She focuses on Camera Synchronization and Neural Rendering. Before that, She got Bachelor's Degree in Computer Science and Technology from Jiangxi Normal University.



Yizhen Lao is an Associate Professor at the College of Computer Science and Electronic Engineering, Hunan University. He obtained PhD degree from University of Clermont-Auvergne, Master's degree in Geo-information Science and Earth Observation from University of Twente and Bachelor's degree in Spatial-Informatics and Digitalized Technology from Wuhan University. His research is focused on 3D computer vision and computational photography.

APPENDIX A

ANALYTICAL JACOBIAN MATRIX

Recall the normalized weighted error term:

$$\hat{\mathbf{e}}_i^j = \Sigma^{-\frac{1}{2}} \mathbf{W}^{-1} \mathbf{C}_i^{j-1} \mathbf{e}_i^j \quad (28)$$

To derive the analytical Jacobian matrix of Eq. (28), we use $\xi_i^j \in \mathfrak{so}(3)$ to parametrize $\mathbf{R}_i^j \in \mathbb{SO}(3)$. The two representations are transformed by Rodrigues formula $\mathbf{R}_i^j = \text{Exp}(\xi_i^j)$ and $\xi_i^j = \text{Log}(\mathbf{R}_i^j)$, we define $\text{Exp}()$ and $\text{Log}()$ as the mapping operator respectively [40]:

$$\begin{aligned} \mathbf{R} &= \text{Exp}(\xi) \\ &= \mathbf{I} + \frac{\sin(\|\xi\|)}{\|\xi\|} \xi^\wedge + \frac{1 - \cos(\|\xi\|)}{\|\xi\|^2} (\xi^\wedge)^2 \end{aligned} \quad (29)$$

$$\begin{aligned} \xi &= \text{Log}(\mathbf{R}) \\ &= \frac{\theta}{2\sin(\theta)} (\mathbf{R} - \mathbf{R}^\top)^\vee \end{aligned} \quad (30)$$

with,

$$\theta = \arccos((\text{tr}(\mathbf{R}) - 1)/2) \quad (31)$$

where \wedge represents the skew symmetric operator that transform a vector to matrix and \vee represent the inverse operator.

The \mathbf{P}_i^c is computed by Eq. (2). Then we get the five atomic partial derivatives of $\partial \hat{\mathbf{e}}_i^j$ over $\partial \mathbf{P}_i$, $\partial \xi^j$, $\partial \mathbf{t}^j$, $\partial \omega^j$ and $\partial \mathbf{d}^j$:

$$\frac{\partial \hat{\mathbf{e}}_i^j}{\partial \mathbf{P}_i} = \Sigma_n^{-\frac{1}{2}} \mathbf{W}^{-1} (\mathbf{C}_i^{j-1} \frac{\partial \mathbf{e}_i^j}{\partial \mathbf{P}_i^c} \frac{\partial \mathbf{P}_i^c}{\partial \mathbf{P}_i} + \begin{bmatrix} \mathbf{e}_i^{j\top} \frac{\partial \mathbf{C}_i^j(1)^{-\top}}{\partial \mathbf{P}_i^c} \\ \mathbf{e}_i^{j\top} \frac{\partial \mathbf{C}_i^j(2)^{-\top}}{\partial \mathbf{P}_i^c} \end{bmatrix}) \quad (32)$$

$$\frac{\partial \hat{\mathbf{e}}_i^j}{\partial \xi^j} = \Sigma_n^{-\frac{1}{2}} \mathbf{W}^{-1} (\mathbf{C}_i^{j-1} \frac{\partial \mathbf{e}_i^j}{\partial \mathbf{P}_i^c} \frac{\partial \mathbf{P}_i^c}{\partial \xi^j} + \begin{bmatrix} \mathbf{e}_i^{j\top} \frac{\partial \mathbf{C}_i^j(1)^{-\top}}{\partial \xi^j} \\ \mathbf{e}_i^{j\top} \frac{\partial \mathbf{C}_i^j(2)^{-\top}}{\partial \xi^j} \end{bmatrix}) \quad (33)$$

$$\frac{\partial \hat{\mathbf{e}}_i^j}{\partial \mathbf{t}^j} = \Sigma_n^{-\frac{1}{2}} \mathbf{W}^{-1} (\mathbf{C}_i^{j-1} \frac{\partial \mathbf{e}_i^j}{\partial \mathbf{P}_i^c} \frac{\partial \mathbf{P}_i^c}{\partial \mathbf{t}^j} + \begin{bmatrix} \mathbf{e}_i^{j\top} \frac{\partial \mathbf{C}_i^j(1)^{-\top}}{\partial \mathbf{t}^j} \\ \mathbf{e}_i^{j\top} \frac{\partial \mathbf{C}_i^j(2)^{-\top}}{\partial \mathbf{t}^j} \end{bmatrix}) \quad (34)$$

$$\frac{\partial \hat{\mathbf{e}}_i^j}{\partial \omega^j} = \Sigma_n^{-\frac{1}{2}} \mathbf{W}^{-1} (\mathbf{C}_i^{j-1} \frac{\partial \mathbf{e}_i^j}{\partial \mathbf{P}_i^c} \frac{\partial \mathbf{P}_i^c}{\partial \omega^j} + \begin{bmatrix} \mathbf{e}_i^{j\top} \frac{\partial \mathbf{C}_i^j(1)^{-\top}}{\partial \omega^j} \\ \mathbf{e}_i^{j\top} \frac{\partial \mathbf{C}_i^j(2)^{-\top}}{\partial \omega^j} \end{bmatrix}) \quad (35)$$

$$\frac{\partial \hat{\mathbf{e}}_i^j}{\partial \mathbf{d}^j} = \Sigma_n^{-\frac{1}{2}} \mathbf{W}^{-1} (\mathbf{C}_i^{j-1} \frac{\partial \mathbf{e}_i^j}{\partial \mathbf{P}_i^c} \frac{\partial \mathbf{P}_i^c}{\partial \mathbf{d}^j} + \begin{bmatrix} \mathbf{e}_i^{j\top} \frac{\partial \mathbf{C}_i^j(1)^{-\top}}{\partial \mathbf{d}^j} \\ \mathbf{e}_i^{j\top} \frac{\partial \mathbf{C}_i^j(2)^{-\top}}{\partial \mathbf{d}^j} \end{bmatrix}) \quad (36)$$

where,

$$\frac{\partial \mathbf{e}_i^j}{\partial \mathbf{P}_i^c} = - \begin{bmatrix} \frac{1}{Z_i^c} & 0 & -\frac{X_i^c}{(Z_i^c)^2} \\ 0 & \frac{1}{Z_i^c} & -\frac{Y_i^c}{(Z_i^c)^2} \end{bmatrix} \quad (37)$$

$$\frac{\partial \mathbf{P}_i^c}{\partial \mathbf{P}_i} = (\mathbf{I} + [\omega^j]_\times r_i^j) \mathbf{R}^j \quad (38)$$

$$\frac{\partial \mathbf{P}_i^c}{\partial \xi^j} = -(\mathbf{I} + [\omega^j]_\times r_i^j) [\mathbf{R}^j \mathbf{P}_i]_\times \quad (39)$$

$$\frac{\partial \mathbf{P}_i^c}{\partial \mathbf{t}^j} = [\mathbf{I}]_{3 \times 3} \quad (40)$$

$$\frac{\partial \mathbf{P}_i^c}{\partial \omega^j} = -r_i^j [\mathbf{R}^j \mathbf{P}_i]_\times \quad (41)$$

$$\frac{\partial \mathbf{P}_i^c}{\partial \mathbf{d}^j} = r_i^j [\mathbf{I}]_{3 \times 3} \quad (42)$$

Note that \mathbf{C}_i^j and \mathbf{W} are defined as:

$$\mathbf{C}_i^j = \begin{bmatrix} 1 & 0 \\ 0 & 1 \end{bmatrix} - \begin{bmatrix} \frac{1}{Z_i^c} & 0 \\ 0 & \frac{1}{Z_i^c} \\ -\frac{X_i^c}{Z_i^{c2}} & -\frac{Y_i^c}{Z_i^{c2}} \end{bmatrix}^\top ([\omega^j]_\times \mathbf{R}^j \mathbf{P}_i + \mathbf{d}^j) \begin{bmatrix} 0 & 1 \end{bmatrix} \quad (43)$$

$$\mathbf{W} = \begin{bmatrix} 1/f_x & 0 \\ 0 & 1/f_y \end{bmatrix} \quad (44)$$

For convenience, we define the following two intermediate variables:

$$\gamma_i^j = \begin{bmatrix} \frac{1}{Z_i^c} & 0 \\ 0 & \frac{1}{Z_i^c} \\ -\frac{X_i^c}{Z_i^{c2}} & -\frac{Y_i^c}{Z_i^{c2}} \end{bmatrix}^\top \quad (45)$$

$$\delta_i^j = [\omega^j]_\times \mathbf{R}^j \mathbf{P}_i + \mathbf{d}^j \quad (46)$$

then we rewrite Eq. (43) as

$$\mathbf{C}_i^j = \begin{bmatrix} 1 & 0 \\ 0 & 1 \end{bmatrix} - \gamma_i^j \delta_i^j \begin{bmatrix} 0 & 1 \end{bmatrix} = \begin{bmatrix} 1 & -\gamma_i^j \delta_i^j \\ 0 & 1 - \gamma_i^j \delta_i^j \end{bmatrix} \quad (47)$$

and its inverse as

$$\mathbf{C}_i^{j-1} = \begin{bmatrix} 1 & \frac{\gamma_i^j \delta_i^j}{1 - \gamma_i^j \delta_i^j} \\ 0 & \frac{1}{1 - \gamma_i^j \delta_i^j} \end{bmatrix} \quad (48)$$

By defining α_i^j and β_i^j as the first and second row of $\gamma_i^j \delta_i^j$ respectively

$$\gamma_i^j \delta_i^j = \begin{bmatrix} \alpha_i^j \\ \beta_i^j \end{bmatrix} \quad (49)$$

we can derive the derivative of \mathbf{C}_i^{j-1} over α_i^j and β_i^j :

$$\frac{\partial \mathbf{C}_i^j(1)^{-\top}}{\partial \mathbf{P}_i} = \begin{bmatrix} [0]_{1 \times 3} \\ (1-\beta_i^j) \frac{\partial \alpha_i^j}{\partial \mathbf{P}_i} + \alpha_i^j \frac{\partial \beta_i^j}{\partial \mathbf{P}_i} \\ (1-\beta_i^j)^2 \end{bmatrix} \quad (50)$$

$$\frac{\partial \mathbf{C}_i^j(2)^{-\top}}{\partial \mathbf{P}_i} = \begin{bmatrix} [0]_{1 \times 3} \\ \frac{\partial \beta_i^j}{\partial \mathbf{P}_i} \\ (1-\beta_i^j)^2 \end{bmatrix} \quad (51)$$

$$\frac{\partial \mathbf{C}_i^j(1)^{-\top}}{\partial \xi^j} = \begin{bmatrix} [0]_{1 \times 3} \\ (1-\beta_i^j) \frac{\partial \alpha_i^j}{\partial \xi^j} + \alpha_i^j \frac{\partial \beta_i^j}{\partial \xi^j} \\ (1-\beta_i^j)^2 \end{bmatrix} \quad (52)$$

$$\frac{\partial \mathbf{C}_i^j(2)^{-\top}}{\partial \xi^j} = \begin{bmatrix} [0]_{1 \times 3} \\ \frac{\partial \beta_i^j}{\partial \xi^j} \\ \frac{\partial \beta_i^j}{(1-\beta_i^j)^2} \end{bmatrix} \quad (53)$$

$$\frac{\partial \mathbf{C}_i^j(1)^{-\top}}{\partial \mathbf{t}^j} = \begin{bmatrix} [0]_{1 \times 3} \\ \frac{(1-\beta_i^j) \frac{\partial \alpha_i^j}{\partial \mathbf{t}^j} + \alpha_i^j \frac{\partial \beta_i^j}{\partial \mathbf{t}^j}}{(1-\beta_i^j)^2} \end{bmatrix} \quad (54)$$

$$\frac{\partial \mathbf{C}_i^j(2)^{-\top}}{\partial \mathbf{t}^j} = \begin{bmatrix} [0]_{1 \times 3} \\ \frac{\partial \beta_i^j}{\partial \mathbf{t}^j} \\ \frac{\partial \beta_i^j}{(1-\beta_i^j)^2} \end{bmatrix} \quad (55)$$

$$\frac{\partial \mathbf{C}_i^j(1)^{-\top}}{\partial \omega^j} = \begin{bmatrix} [0]_{1 \times 3} \\ \frac{(1-\beta_i^j) \frac{\partial \alpha_i^j}{\partial \omega^j} + \alpha_i^j \frac{\partial \beta_i^j}{\partial \omega^j}}{(1-\beta_i^j)^2} \end{bmatrix} \quad (56)$$

$$\frac{\partial \mathbf{C}_i^j(2)^{-\top}}{\partial \omega^j} = \begin{bmatrix} [0]_{1 \times 3} \\ \frac{\partial \beta_i^j}{\partial \omega^j} \\ \frac{\partial \beta_i^j}{(1-\beta_i^j)^2} \end{bmatrix} \quad (57)$$

$$\frac{\partial \mathbf{C}_i^j(1)^{-\top}}{\partial \mathbf{d}^j} = \begin{bmatrix} [0]_{1 \times 3} \\ \frac{(1-\beta_i^j) \frac{\partial \alpha_i^j}{\partial \mathbf{d}^j} + \alpha_i^j \frac{\partial \beta_i^j}{\partial \mathbf{d}^j}}{(1-\beta_i^j)^2} \end{bmatrix} \quad (58)$$

$$\frac{\partial \mathbf{C}_i^j(2)^{-\top}}{\partial \mathbf{d}^j} = \begin{bmatrix} [0]_{1 \times 3} \\ \frac{\partial \beta_i^j}{\partial \mathbf{d}^j} \\ \frac{\partial \beta_i^j}{(1-\beta_i^j)^2} \end{bmatrix} \quad (59)$$

where $\mathbf{C}(1)$ and $\mathbf{C}(2)$ are the first and second row of \mathbf{C} respectively. Then we can derive the derivative of α_i^j and β_i^j over $\partial \hat{\mathbf{e}}_i^j$ over $\partial \mathbf{P}_i$, $\partial \xi^j$, $\partial \mathbf{t}^j$, $\partial \omega^j$ and $\partial \mathbf{d}^j$:

$$\frac{\partial(\gamma_i^j \delta_i^j)}{\partial \mathbf{P}_i} = \gamma_i^j \frac{\partial \delta_i^j}{\partial \mathbf{P}_i} + \begin{bmatrix} \delta_i^j \top \frac{\partial \gamma_i^j(1)^\top}{\partial \mathbf{P}_i^c} \frac{\partial \mathbf{P}_i^c}{\partial \mathbf{P}_i} \\ \delta_i^j \top \frac{\partial \gamma_i^j(2)^\top}{\partial \mathbf{P}_i^c} \frac{\partial \mathbf{P}_i^c}{\partial \mathbf{P}_i} \end{bmatrix} \quad (60)$$

$$\frac{\partial(\gamma_i^j \delta_i^j)}{\partial \xi^j} = \gamma_i^j \frac{\partial \delta_i^j}{\partial \xi^j} + \begin{bmatrix} \delta_i^j \top \frac{\partial \gamma_i^j(1)^\top}{\partial \mathbf{P}_i^c} \frac{\partial \mathbf{P}_i^c}{\partial \xi^j} \\ \delta_i^j \top \frac{\partial \gamma_i^j(2)^\top}{\partial \mathbf{P}_i^c} \frac{\partial \mathbf{P}_i^c}{\partial \xi^j} \end{bmatrix} \quad (61)$$

$$\frac{\partial(\gamma_i^j \delta_i^j)}{\partial \mathbf{t}^j} = \gamma_i^j \frac{\partial \delta_i^j}{\partial \mathbf{t}^j} + \begin{bmatrix} \delta_i^j \top \frac{\partial \gamma_i^j(1)^\top}{\partial \mathbf{P}_i^c} \frac{\partial \mathbf{P}_i^c}{\partial \mathbf{t}^j} \\ \delta_i^j \top \frac{\partial \gamma_i^j(2)^\top}{\partial \mathbf{P}_i^c} \frac{\partial \mathbf{P}_i^c}{\partial \mathbf{t}^j} \end{bmatrix} \quad (62)$$

$$\frac{\partial(\gamma_i^j \delta_i^j)}{\partial \omega^j} = \gamma_i^j \frac{\partial \delta_i^j}{\partial \omega^j} + \begin{bmatrix} \delta_i^j \top \frac{\partial \gamma_i^j(1)^\top}{\partial \mathbf{P}_i^c} \frac{\partial \mathbf{P}_i^c}{\partial \omega^j} \\ \delta_i^j \top \frac{\partial \gamma_i^j(2)^\top}{\partial \mathbf{P}_i^c} \frac{\partial \mathbf{P}_i^c}{\partial \omega^j} \end{bmatrix} \quad (63)$$

$$\frac{\partial(\gamma_i^j \delta_i^j)}{\partial \mathbf{d}^j} = \gamma_i^j \frac{\partial \delta_i^j}{\partial \mathbf{d}^j} + \begin{bmatrix} \delta_i^j \top \frac{\partial \gamma_i^j(1)^\top}{\partial \mathbf{P}_i^c} \frac{\partial \mathbf{P}_i^c}{\partial \mathbf{d}^j} \\ \delta_i^j \top \frac{\partial \gamma_i^j(2)^\top}{\partial \mathbf{P}_i^c} \frac{\partial \mathbf{P}_i^c}{\partial \mathbf{d}^j} \end{bmatrix} \quad (64)$$

where,

$$\frac{\partial \gamma_i^j(1)^\top}{\partial \mathbf{P}_i^c} = \begin{bmatrix} 0 & 0 & -\frac{1}{Z_i^{c2}} \\ 0 & 0 & 0 \\ -\frac{1}{Z_i^{c2}} & 0 & \frac{2X_i^c}{Z_i^{c3}} \end{bmatrix} \quad (65)$$

$$\frac{\partial \gamma_i^j(2)^\top}{\partial \mathbf{P}_i^c} = \begin{bmatrix} 0 & 0 & 0 \\ 0 & 0 & -\frac{1}{Z_i^{c2}} \\ 0 & -\frac{1}{Z_i^{c2}} & \frac{2Y_i^c}{Z_i^{c3}} \end{bmatrix} \quad (66)$$

$$\frac{\partial \delta_i^j}{\partial \mathbf{P}_i} = [\omega^j]_{\times} \mathbf{R}^j \quad (67)$$

$$\frac{\partial \delta_i^j}{\partial \xi^j} = [\omega^j]_{\times} [\mathbf{R}^j \mathbf{P}_i]_{\times} \quad (68)$$

$$\frac{\partial \delta_i^j}{\partial \mathbf{t}^j} = [0]_{3 \times 3} \quad (69)$$

$$\frac{\partial \delta_i^j}{\partial \omega^j} = -[\mathbf{R}^j \mathbf{P}_i]_{\times} \quad (70)$$

$$\frac{\partial \delta_i^j}{\partial \mathbf{d}^j} = [\mathbf{I}]_{3 \times 3} \quad (71)$$

APPENDIX B

THE EQUIVALENT BETWEEN NORMALIZED DC-RSBA AND NW-RSBA

Recalling the Eq. 16, it is interesting to define a new vector χ_i^j

$$\chi_i^j = \frac{\partial \Pi(\mathbf{R}^j(r_i^j) \mathbf{P}_i + \mathbf{t}^j(r_i^j))}{\partial n_r} = \frac{\partial \Pi(\mathbf{R}^j(r_i^j) \mathbf{P}_i + \mathbf{t}^j(r_i^j))}{\partial \tilde{r}_i^j} \quad (72)$$

then we can reformulate Eq. 47

$$\mathbf{C}_i^j = \begin{bmatrix} 1 & 0 \\ 0 & 1 \end{bmatrix} - \frac{\partial \Pi(\mathbf{R}^j(r_i^j) \mathbf{P}_i + \mathbf{t}^j(r_i^j))}{\partial n_r} \begin{bmatrix} 0 & 1 \end{bmatrix} = \begin{bmatrix} 1 & -\chi_i^{j(1)} \\ 0 & 1 - \chi_i^{j(2)} \end{bmatrix} \quad (73)$$

$$\mathbf{C}_i^{j-1} = \begin{bmatrix} 1 & \frac{\chi_i^{j(1)}}{1 - \chi_i^{j(2)}} \\ 0 & \frac{1}{1 - \chi_i^{j(2)}} \end{bmatrix} \quad (74)$$

define the rectified image coordinate vector $\begin{bmatrix} c_i^{j''} & r_i^{j''} \end{bmatrix}^\top$ which represents the exact coordinate after Eq. 19

$$\begin{bmatrix} \tilde{c}_i^j \\ \tilde{r}_i^j \end{bmatrix} - \begin{bmatrix} c_i^{j''} \\ r_i^{j''} \end{bmatrix} = \mathbf{C}_i^{j-1} \left(\begin{bmatrix} \tilde{c}_i^j \\ \tilde{r}_i^j \end{bmatrix} - \begin{bmatrix} c_i^{j''} \\ r_i^{j''} \end{bmatrix} \right) \quad (75)$$

our goal is to prove that using rectified coordinate as the observed image coordinate will project on the same image coordinate, by normalized measurement based projection Eq. 5

$$\begin{bmatrix} c_i^{j''} & r_i^{j''} & 1 \end{bmatrix}^\top = \Pi(\mathbf{R}^j(r_i^{j''}) \mathbf{P}_i + \mathbf{t}^j(r_i^{j''})) \quad (76)$$

which also known as the rolling shutter camera constraint then we start to prove c and r consequently, we follow the schedule that firstly solve the Eq. 76 then using Eq. 5 to get

the projection coordinate and check out whether it is the same. first prove r

$$(1 - \chi_i^{j(2)})(\tilde{r}_i^j - r_i^j) = (\tilde{r}_i^j - r_i^j) \quad (77)$$

$$\begin{aligned} r_i^{j''} &= \frac{r_i^j - \chi_i^{j(2)} \tilde{r}_i^j}{1 - \chi_i^{j(2)}} \\ &= r_i^j + \frac{\chi_i^{j(2)}(r_i^j - \tilde{r}_i^j)}{1 - \chi_i^{j(2)}} \\ &= \tilde{r}_i^j + \frac{r_i^j - \tilde{r}_i^j}{1 - \chi_i^{j(2)}} \end{aligned} \quad (78)$$

$$\begin{aligned} r_i^{jnew} &= \pi(\mathbf{P}_i, \mathbf{R}^j, \mathbf{t}^j, \omega^j, \mathbf{d}^j, r_i^{j''})^{(2)} \\ &= \pi(\mathbf{P}_i, \mathbf{R}^j, \mathbf{t}^j, \omega^j, \mathbf{d}^j, \tilde{r}_i^j + \frac{r_i^j - \tilde{r}_i^j}{1 - \chi_i^{j(2)}})^{(2)} \\ &= r_i^j + \left(\frac{\partial \pi(\mathbf{P}_i, \mathbf{R}^j, \mathbf{t}^j, \omega^j, \mathbf{d}^j, \tilde{r}_i^j)}{\partial \tilde{r}_i^j} \right)^{(2)} \frac{r_i^j - \tilde{r}_i^j}{1 - \chi_i^{j(2)}} \\ &= r_i^j + \frac{\chi_i^{j(2)}(r_i^j - \tilde{r}_i^j)}{1 - \chi_i^{j(2)}} \\ &= r_i^{j''} \end{aligned} \quad (79)$$

then we prove c

$$(\tilde{c}_i^j - c_i^{j''}) = \frac{\chi_i^{j(1)}}{1 - \chi_i^{j(2)}}(\tilde{r}_i^j - r_i^j) + (\tilde{c}_i^j - c_i^j) \quad (80)$$

$$c_i^{j''} = c_i^j - \frac{\chi_i^{j(1)}}{1 - \chi_i^{j(2)}}(\tilde{r}_i^j - r_i^j) \quad (81)$$

$$\begin{aligned} c_i^{jnew} &= \pi(\mathbf{P}_i, \mathbf{R}^j, \mathbf{t}^j, \omega^j, \mathbf{d}^j, r_i^{j''})^{(1)} \\ &= \pi(\mathbf{P}_i, \mathbf{R}^j, \mathbf{t}^j, \omega^j, \mathbf{d}^j, \tilde{r}_i^j + \frac{r_i^j - \tilde{r}_i^j}{1 - \chi_i^{j(2)}})^{(1)} \\ &= c_i^j + \left(\frac{\partial \pi(\mathbf{P}_i, \mathbf{R}^j, \mathbf{t}^j, \omega^j, \mathbf{d}^j, \tilde{r}_i^j)}{\partial \tilde{r}_i^j} \right)^{(1)} \frac{r_i^j - \tilde{r}_i^j}{1 - \chi_i^{j(2)}} \\ &= c_i^j + \frac{\chi_i^{j(1)}}{1 - \chi_i^{j(2)}}(r_i^j - \tilde{r}_i^j) \\ &= c_i^j - \frac{\chi_i^{j(1)}}{1 - \chi_i^{j(2)}}(\tilde{r}_i^j - r_i^j) \\ &= c_i^{j''} \end{aligned} \quad (82)$$

combining Eq. 79 and Eq. 82, we can get such summary that Normalized DC-RSBA is equivalent to NW-RSBA mathematical.